Applications of DECIDE Quantum-Classical Dynamics: Proton Transfer and Quantum Battery Models

by

Zhe Liu

A thesis submitted in partial fulfillment of the requirements for the degree of

Master of Science

Department of Chemistry
University of Alberta

Abstract

The quantum-classical Liouville equation (QCLE) provides a foundation for simulating the dynamics of quantum systems coupled to classical environments. Many processes including proton-transfer reactions, electron-transfer reactions, and heat transport in molecular junctions, for example, take place in such mixed quantum-classical systems. The most accurate algorithms for solving the QCLE require very large ensembles of trajectories to obtain converged results, which is computationally prohibitive for many systems. The recently developed "Deterministic evolution of coordinates with initial decoupled equations" (DECIDE) method has demonstrated promise in solving the QCLE with high accuracy and low computational cost for several model systems; however, its broad scale applicability is still under investigation.

Previously, the applications of DECIDE relied on subsystem and adiabatic energy basis representations. While these representations are convenient for certain systems, the position representation is convenient for many other systems, including systems undergoing proton- and electron-transfer reactions. Thus, as a starting point, we cast the DECIDE equations of motion for a simple one-dimensional proton-transfer model in a finite quantum harmonic oscillator position basis. After solving the

DECIDE equations of motion in this basis, we showed that it is possible to generate trajectories that conserve the total energy of the system and we calculated various quantities of interest. Next, we considered a two-dimensional proton-transfer model. In this case, it was not possible to generate trajectories that conserve energy out to arbitrary times. Our analysis revealed that the finite nature of the position basis and the order of the Hamiltonian are responsible for the accumulation of numerical errors that ultimately lead to a breakdown of energy conservation.

In a recent study, our group proposed a novel platform for an open excitonic quantum battery (EQB), which takes advantage of a symmetry-protected dark state residing in a decoherence-free subspace. While in this dark state, the EQB can store an exciton for an indefinite period of time without any environment-induced population losses (known as the storage phase). When a symmetry-breaking perturbation is connected to the EQB, the battery begins to discharge the exciton (known as the discharge phase). In this thesis, we demonstrated that the quantum battery is not only loss-free with respect to exciton population during the storage phase, but also with respect to the battery energy. We then went on to explore the population and energy dynamics of the battery during the discharge phase over a wide range of parameter regimes – site energies, bath temperatures, and bath reorganization energies. Our results shed light on how to control the rate/amount of population and/or energy from the battery.

Preface

The candidate confirms that the work submitted is his/her own and that appropriate credit has been given where reference has been made to the work of others.

This copy has been supplied on the understanding that it is copyright material and that no quotation from the thesis may be published without proper acknowledgement.

The right of Zhe Liu to be identified as Author of this work has been asserted by him/her in accordance with the Copyright, Designs and Patents Act 1988.

To my family and friends.

QUAECUMQUE VERA

Acknowledgements

First of all, I would like to thank my supervisor, Professor Gabriel Hanna, for his kindness, encouragement, helpfulness, consideration, patience, and knowledge. It has been a fulfilling experience working under his supervision. He has been a great role model to me.

I would also like to thank my family and friends for all their support.

Thank you to my M.Sc. defense and supervisory committee members, Professor Phillip Choi, Professor Sheref S. Mansy, and Professor Yunjie Xu.

I am grateful for the research experience with Professor Kai Leonhard, and support from Lukas Krep and Rene Seyfarth at RWTH Aachen University.

Thank you to Professor Alex Brown, Professor Julianne Gibbs, and Professor Tian Tang for their help in my career development.

Thank you to my fellow group members, Pablo Carpio Martinez, Craig Peeples, Negin Razavilar, Zohreh Khodadad, and Yifei Zhang.

Last but not least, I am grateful for financial support from the Mitacs Globalink Graduate Fellowship and the RWTH Aachen - University of Alberta Junior Research Fellowship.

Contents

List of Tables

List of Figures

Chapter 1

Introduction

Most systems of interest in chemistry and biology contain very large numbers of degrees of freedom (DOF). An exact simulation of the dynamics of such a system requires a fully quantum mechanical treatment of the entire system, which is computationally prohibitive due to the exponential scaling with the number of DOF. One approach to overcoming this issue is to treat a few degrees of freedom of interest quantum mechanically (i.e., subsystem) and the remainder classically (i.e., environment or bath) [1, 2, 3]. Within this approach, the quantum subsystem is described in terms of a Hilbert space and the classical environment in terms of a phase space of positions and momenta. Previously, these *mixed quantum-classical* techniques have been applied to a wide range of phenomena, e.g., proton transfer reactions [4, 5], electron transfer reactions [6, 7], proton-coupled electron transfer reactions [8, 9, 10, 11, 12, 13, 14], exciton transport in photosynthetic complexes [15, 16, 17], and heat transport in molecular junctions [18, 19, 20, 21], etc.

The quantum-classical Liouville equation (QCLE) serves as a starting point for simulating the dynamics of mixed quantum-classical systems [2, 3, 22]. Over the years, a host of techniques have been developed based on approximate solutions of the QCLE [4, 3, 23, 16, 22, 24]. The most accurate of these techniques are the so-called stochastic surface-hopping solutions [4, 23], but they require extremely large ensembles of trajectories to obtain converged results and, as a result, will be computationally prohibitive for many systems. On the other hand, the Poisson Bracket

Mapping Equation (PBME) approach provides a highly computationally efficient approximate solution of the QCLE, but its applicability is mainly restricted to systems with weak subsystem-bath couplings [25, 26, 6, 27]. Recently, the "Deterministic evolution of coordinates with initial decoupled equations" (DECIDE) method was developed, which offers a favourable balance between computational economy and accuracy [24]. DECIDE has two main advantages compared to the stochastic QCLE-based methods: (i) It is a deterministic method that requires the integration of $L^2(L^2 - 2 + 2N)$ coupled differential equations (where L is the number of basis functions used to represent the subsystem and N is the number of environmental DOF). Typically, only a few thousand trajectories are required to obtain converged results, in contrast to several orders of magnitude more trajectories in the case of the stochastic QCLE-based methods; (ii) There is no need to diagonalize the Hamiltonian matrix on-the-fly. DECIDE has demonstrated great promise in solving the QCLE with high accuracy and low computational cost for a number of model systems, including the spin-boson model [24, 28], Fenna-Matthews-Olson model [24, 28], a three-state photo-induced electron transfer model [24], nonequilibrium spin-boson model [19, 20, 29], and a quantum battery model [30].

To date, the DECIDE equations have been represented in *complete* spin, subsystem, and adiabatic *energy* bases, and successfully applied to simulating the dynamics of Hamiltonians expressed in these bases. However, the feasibility of expressing the DECIDE equations in a *finite position* basis has yet to be explored. In this thesis, we represent the DECIDE equations in a quantum harmonic oscillator basis and use the resulting equations to simulate the dynamics of one- and two-dimensional models [31] of proton transfer reactions.

In a recent study by our group, we simulated the exciton population dynamics of an open quantum network model of a charged excitonic quantum battery (EQB) [30]. By initializing the EQB in a symmetry-protected dark state, it was possible to store an exciton indefinitely without any loss to the surrounding thermal baths. Moreover, it was shown that the exciton could be discharged by breaking the symmetry of the EQB. In this thesis, we use the DECIDE method to study both the exciton population and energy dynamics of this quantum battery model across a wide range

of parameter regimes, viz., site energies, bath temperatures, and bath reorganization energies.

The thesis is organized as follows. In Chapter 2, we first discuss the Wigner-Weyl transform, which has been widely used in mixed quantum-classical dynamics, as it provides an invertible mapping between Hilbert space operators and phase space functions. In particular, we introduce the partial Wigner-Weyl transform to the bath DOF, which retains a Hilbert space description of the quantum subsystem. Then, we derive the QCLE, which is the starting point for the development of a host of mixed quantum-classical dynamics methods. At the end of the chapter, we derive the DECIDE equations of motion and briefly discuss their underlying approximations and energy conservation. In Chapter 3, we explore the ability of the DECIDE method for simulating the dynamics of one- and two-dimensional proton transfer models in a finite position basis. In Chapter 4, we study the exciton population and energy transfer dynamics of a model quantum battery over a wide range of parameter regimes, using the DECIDE method. Finally, we summarize our findings and propose ideas for future work in Chapter 5.

Chapter 2

Mixed Quantum-Classical Dynamics

2.1 Wigner-Weyl transform

The Wigner-Weyl transform was first introduced by Wigner in 1932 [32]. Wigner's original goal was to find correction terms that would bridge quantum and classical mechanics [33, 32]. The transform can be understood in terms of probability functions. For example, for a given wave function in position space, $\psi(x)$, the probability density is $|\psi(x)|^2$. The wave function can also be expressed in momentum space as

$$\phi(p) = \frac{1}{\sqrt{h}} \int e^{-ixp/\hbar} \psi(x)\ dx = \langle p|\psi\rangle\,, \tag{2.1}$$

where $\hbar = h/2\pi$ (h is Planck's constant) and the associated probability density is $|\phi(p)|^2$. Both expressions above depend on a single variable, either x or p. The Wigner-Weyl transform provides a way to represent the probability distribution in terms of position (x) and momentum (p) simultaneously. By definition, the Wigner-Weyl transform of an operator $\hat{A}$ is

$$\begin{aligned} A_W(x,p) &= \int e^{-ipy/\hbar} \psi^*(x+\frac{y}{2}) \hat{A} \psi(x-\frac{y}{2})\ dy, \\ &= \int e^{-ipy/\hbar} \left\langle x+\frac{y}{2}|\hat{A}|x-\frac{y}{2}\right\rangle\ dy, \end{aligned} \tag{2.2}$$

where x and p are vectors containing the positions and momenta of all DOF in the system and y is an arbitrary integration variable.

Using the above definition, one can derive several properties of this transformation. First, for the identity operator $\hat{1}$,

$$\begin{aligned} 1_W &= \int e^{-ipy/\hbar} \left\langle x + \frac{y}{2} | \hat{1} | x - \frac{y}{2} \right\rangle \, dy \\ &= \int e^{-ipy/\hbar} \delta(x + \frac{y}{2} - x + \frac{y}{2}) \, dy = 1. \end{aligned} \tag{2.3}$$

Second, for an operator $\hat{A}$ that is only a function of $\hat{x}$, the Wigner-Weyl transform is

$$\begin{aligned} A_W(x) &= \int e^{-ipy/\hbar} \left\langle x + \frac{y}{2} | \hat{A} | x - \frac{y}{2} \right\rangle \, dy \\ &= \int e^{-ipy/\hbar} A(x - \frac{y}{2}) \delta(y) \, dy. \end{aligned} \tag{2.4}$$

Similarly, for an operator $\hat{A}$ that is only a function of $\hat{p}$, its Wigner-Weyl transform is $A(p)$. Third, the trace of the product of two operators $\hat{A}$ and $\hat{B}$ is

$$\mathrm{Tr}(\hat{A}\hat{B}) = \frac{1}{h} \int \int A_W(x,p) B_W(x,p) \, dxdp. \tag{2.5}$$

The Wigner function, which corresponds to the probability density of x and p, is defined in terms of the density operator $\hat{\rho} = |\psi\rangle\langle\psi|$ as

$$\rho_W(x,p)/h = \frac{1}{h} \int \int e^{-ipy\hbar} |x + \frac{y}{2}\rangle\langle x - \frac{y}{2}| \, dxdy \equiv W(x,p). \tag{2.6}$$

For example, the Wigner functions for the ground and first-excited states of the quantum harmonic oscillator are shown in Fig. 2.1. The expectation value of a Wigner-Weyl-transformed operator $\hat{A}$ is given by

$$\langle \hat{A} \rangle = \mathrm{Tr}(\hat{\rho}\hat{A}) = \int \int W(x,p) A_W(x,p) \, dxdp. \tag{2.7}$$

For a Hamiltonian $\hat{H} = T(\hat{p}) + U(\hat{x})$, where T is the kinetic energy and U is the

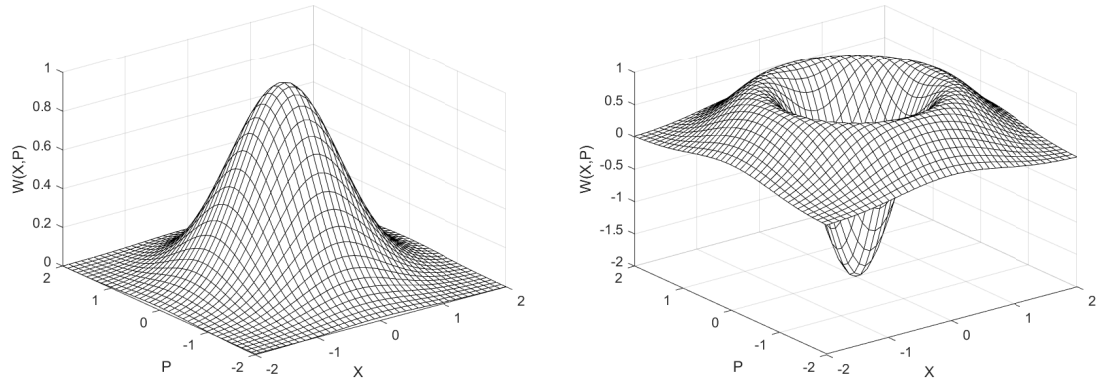

Figure 2.1: Wigner functions for the (a) ground state, $W_0(x,p) = 2\exp(-p^2 - x^2)$, and (b) excited state, $W_1(x,p) = 2(-1+2p^2+2x^2)\exp(-p^2-x^2)$, of the dimensionless quantum harmonic oscillator ($\hat{H} = -\frac{1}{2}\frac{d^2}{dx^2} + \frac{1}{2}x^2$). The expressions for the Wigner functions are taken from Ref. [33].

potential energy, the expectation values of $T(\hat{p})$ and $U(\hat{x})$ are

$$\langle T \rangle = \iint W(x,p) T_W(p)\ dxdp, \tag{2.8}$$

and

$$\langle U \rangle = \iint W(x,p) U_W(x)\ dxdp. \tag{2.9}$$

$W(x,p)$ is normalized, i.e.,

$$\int\int W(x,p)\ dxdp = \mathrm{Tr}(\rho) = 1. \tag{2.10}$$

The Wigner-Weyl transform of the product of two operators is [34]

$$(\hat{A}\hat{B})_W = A_W(x,p)\exp\left(\hbar\Lambda/2i\right)B_W(x,p) \equiv A_W(x,p) * B_W(x,p). \tag{2.11}$$

In the above equation, $*$ denotes the Moyal star product [35, 36] and Λ is the Poisson

bracket operator,

$$\Lambda = \frac{\overleftarrow{\partial}}{\partial p} \cdot \frac{\overrightarrow{\partial}}{\partial x} - \frac{\overleftarrow{\partial}}{\partial p} \cdot \frac{\overrightarrow{\partial}}{\partial x}, \tag{2.12}$$

where the arrows denote the directions of the operator. (The derivation of Eq. 2.11 may be found in Ref. [34].) The exponential in Eq. 2.11 may be expanded in the following series,

$$e^{\hbar\Lambda/2i} = 1 + \frac{\hbar}{2i}\Lambda + \left(\frac{\hbar}{2i}\Lambda\right)^2 /2! + \ldots. \tag{2.13}$$

Another useful expression is the Wigner transform of the Boltzmann operator $\Omega \equiv e^{-\beta H}$, where $\beta = 1/kT$ [34, 37]. For a canonical ensemble in equilibrium, the probability of a specific state is proportional to Ω. For example, let us consider a system containing one harmonic oscillator whose Hamiltonian is

$$\hat{H} = \frac{\hat{p}^2}{2} + \frac{1}{2}\omega^2\hat{x}^2, \tag{2.14}$$

where $\hat{x}$ and $\hat{p}$ are the mass-weighted position and momentum operators, respectively. The Wigner-Weyl transform of Ω may be obtained as follows. Consider the derivative of Ω with respect to β,

$$\frac{\partial\Omega}{\partial\beta} = -\hat{H}\Omega. \tag{2.15}$$

Taking the Wigner-Weyl transform of both sides of this equation, we obtain

$$\frac{\partial\Omega_W}{\partial\beta} = -H_W \exp\left(\hbar\Lambda/2i\right)\Omega_W. \tag{2.16}$$

Since $\Omega_W(\beta = 0) = 1$, Eq. 2.16 becomes

$$\frac{\partial\Omega_W}{\partial\beta} = -H_W \cos\left(\hbar\Lambda/2\right)\Omega_W, \tag{2.17}$$

which is also known as the Bloch equation. Inserting the expression for $\hat{H}$ in Eq. 2.14

into Eq. 2.16, we obtain

$$\frac{\partial \Omega_W}{\partial \beta} = -H_W \Omega_W + (\hbar^2/8)\left[\frac{\partial^2}{\partial x^2} + \omega^2 \frac{\partial^2}{\partial p^2}\right] \Omega_W. \tag{2.18}$$

To arrive at Eq. 2.18, the second-order expansion of Eq. 2.13 was used with the first-order term omitted because $\Omega_W(\beta = 0) = 1$. Then, one assumes a solution for Ω_W of the form,

$$\Omega_W = \exp\left[-A(\beta) H_W + B(\beta)\right]. \tag{2.19}$$

Therefore,

$$\frac{dA(\beta)}{d\beta} H_W + \frac{dB(\beta)}{d\beta} = -H_W - \frac{1}{4}\hbar^2\omega^2 A + \frac{1}{4}\hbar^2\omega^2 H_W. \tag{2.20}$$

By comparing the coefficients, one finds

$$A = (2/\hbar\omega)\tanh \hbar\omega\beta/2, \tag{2.21}$$

$$B = -\ln\cosh \hbar\omega\beta/2. \tag{2.22}$$

Then, the probability of the harmonic oscillator being at x and p (setting $\hbar = 1$) is

$$\rho = \frac{\tanh \beta\omega/2}{\pi} \exp\left[-\frac{2\tanh(\beta\omega/2)}{\omega}\left(\frac{p^2}{2} + \frac{\omega x^2}{2}\right)\right]. \tag{2.23}$$

Finally, for a set of N harmonic oscillators,

$$\rho = \prod_{j=1}^{N} \frac{\tanh \beta\omega_j/2}{\pi} \exp\left[-\frac{2\tanh(\beta\omega_j/2)}{\omega_j}\left(\frac{p^2}{2} + \frac{\omega_j x^2}{2}\right)\right]. \tag{2.24}$$

2.2 Quantum-Classical Liouville Equation

In this section, we derive the quantum-classical Liouville equation (QCLE) [2, 3, 22], which has been used as the starting point for deriving a host of mixed quantum-classical dynamics techniques. The derivation begins with the quantum Liouville

equation for the density operator of a quantum system,

$$\frac{\partial \hat{\rho}}{\partial t} = -\frac{i}{\hbar}\left[\hat{H}, \hat{\rho}\right], \tag{2.25}$$

where $[\cdots]$ denotes a commutator. Since a mixed quantum-classical system is composed of a quantum subsystem that is coupled to a classical bath (or environment), one then applies a partial Wigner-Weyl transform over the bath DOF to the quantum Liouville equation to obtain

$$\begin{aligned} \frac{\partial \hat{\rho}_W(R,P,t)}{\partial t} &= -\frac{i}{\hbar}((\hat{H}\hat{\rho})_W - (\hat{\rho}\hat{H})_W) \qquad (2.26)\\ &= -\frac{i}{\hbar}(\hat{H}_W(R,P)e^{\hbar\Lambda/2i}\hat{\rho}_W(R,P,t) - \hat{\rho}_W(R,P,t)e^{\hbar\Lambda/2i}\hat{H}_W(R,P)), \end{aligned}$$

where R and P are vectors containing the positions and momenta, respectively, of the classical DOF. Before carrying out the next step, we introduce several dimensionless variables. This is done by first defining an arbitrary energy unit ϵ_0, such that the time unit becomes $t_0 = \hbar/\epsilon_0$ and the length unit becomes $\lambda_m = (\hbar^2/m\epsilon)^{1/2}$. Using these units, the dimensionless variables are

$$\begin{aligned} \hat{q}' &= \hat{q}/\lambda, & R' &= R/\lambda_m \\ \hat{p}' &= \hat{p}'/(m\lambda_m/t_0) = \hat{p}'/(m\epsilon_0)^{1/2}, & P' &= P/(M\epsilon_0)^{1/2}, \end{aligned} \tag{2.27}$$

where m and M denote the masses of the quantum and classical DOF, respectively. In terms of the dimensionless variables, Eq. 2.26 becomes

$$\frac{\partial \hat{\rho}'_W(R',P',t')}{\partial t'} = -i(\hat{H}'_W(R',P')e^{\mu\Lambda/2i}\hat{\rho}'_W(R',P',t') - \rho'_W(R',P',t')e^{\mu\Lambda/2i}\hat{H}'_W(R',P')), \tag{2.28}$$

where $\mu = (m/M)^{1/2}$. Expanding Eq. 2.28 and keeping only up to first-order terms in μ (since it is assumed that the subsystem DOF are much lighter than the bath

DOF and, thus, higher order terms in μ are very small), one obtains

$$\begin{aligned}\frac{\partial \hat{\rho}'_W(R,P,t)}{\partial t} &= -i\left[\hat{H}'_W(R',P'),\hat{\rho}'_W(R',P',t')\right] \\ &+\frac{\mu}{2}\left(\{\hat{H}'_W(R',P'),\hat{\rho}'_W(R',P',t')\}-\{\hat{\rho}'_W(R',P'),\hat{H}'_W(R',P',t')\}\right).\end{aligned} \tag{2.29}$$

Switching back to unscaled variables, one obtains

$$\begin{aligned}\frac{\partial \hat{\rho}_W(R,P,t)}{\partial t} &= -\frac{i}{\hbar}\left[\hat{H}_W(R,P),\hat{\rho}_W(R,P,t)\right] \\ &+\frac{1}{2}\left(\{\hat{H}_W(R,P),\hat{\rho}_W(R,P,t)\}-\{\hat{\rho}_W(R,P),\hat{H}_W(R,P,t)\}\right),\end{aligned} \tag{2.30}$$

which is known as the QCLE. Defining the quantum-classical Liouville operator $\mathcal{L}_W$, one may conveniently write the QCLE as

$$\frac{\partial \hat{\rho}_W(R,P,t)}{\partial t} \equiv -i\mathcal{L}_W\hat{\rho}_W(R,P,t). \tag{2.31}$$

One can also derive an analogous equation for any observable in the Heisenberg picture, namely

$$\frac{\partial \hat{A}_W(R,P,t)}{\partial t} = i\mathcal{L}_W\hat{A}_W(R,P,t). \tag{2.32}$$

To solve the QCLE, one must first choose a basis for the Hilbert space of the quantum subsystem. For example, for a system with the following general Hamiltonian,

$$\hat{H}_W(R,P) = \frac{P^2}{2M}+\frac{\hat{p}^2}{2m}+\hat{V}_W(\hat{q},R) \equiv \frac{P^2}{2M}+\hat{h}_W(R), \tag{2.33}$$

where $\hat{h}_W(R) = \frac{\hat{p}^2}{2m}+\hat{V}_W(\hat{q},R)$, one may choose the eigenstates of $\hat{h}_W(R)$ as the basis. This basis is often referred to as the *adiabatic* basis. Taking matrix elements

of both sides of the QCLE using this basis, one obtains [2]

$$\begin{aligned}\frac{\partial \rho_W^{\alpha\alpha'}(R,P,t)}{\partial t} &= -i\omega_{\alpha,\alpha'}(R)\rho_W^{\alpha\alpha'}(R,P,t) \\ &+\frac{1}{2}\sum_{\alpha''}\frac{P}{M}\left(\rho_W^{\alpha\alpha''}d_{\alpha''\alpha'} - d_{\alpha\alpha''}\rho_W^{\alpha''\alpha'}\right) - \frac{P}{M}\frac{\partial \rho_W^{\alpha\alpha'}}{\partial R} \\ &-\frac{1}{2}\sum_{\alpha''}\left(F_W^{\alpha\alpha''}\frac{\partial \rho_W^{\alpha''\alpha'}}{\partial P} + \frac{\partial \rho_W^{\alpha\alpha''}}{\partial P}F_W^{\alpha''\alpha'}\right), \end{aligned} \tag{2.34}$$

where $\omega_{\alpha\alpha'}(R) = [E_\alpha(R) - E_{\alpha'}(R)]/\hbar$ is the transition frequency between adiabatic states $|\alpha\rangle$ and $|\alpha'\rangle$, $d_{\alpha\alpha'} = \left\langle \alpha; R|\frac{\partial}{\partial R}|\alpha'; R\right\rangle$ is the nonadiabatic coupling vector, and $F_W^{\alpha\alpha'} = -\left\langle \alpha; R|\frac{\partial \hat{V}_W(\hat{q},R)}{\partial R}|\alpha'; R\right\rangle$ is the Hellmann-Feynman force acting on the classical DOF.

2.3 The DECIDE Approach

In this section, we derive the DECIDE equations of motion [24]. Let us start by considering a fully quantum system with a time-independent Hamiltonian, whose subsystem and bath coordinates are denoted by $\hat{x}$ and $\hat{X}$, respectively. In the Heisenberg picture, the dynamics of the subsystem and bath coordinates are given by the quantum Liouville equation, namely

$$\begin{aligned}\frac{d}{dt}\hat{x}(t) &= \frac{i}{\hbar}\left[\hat{H}, \hat{x}(t)\right] = \frac{i}{\hbar}e^{i\hat{\mathcal{L}}^Q t}\left[\hat{H}, \hat{x}\right] \equiv \frac{i}{\hbar}\left(\left[\hat{H}, \hat{x}\right]\right)(t) \\ \frac{d}{dt}\hat{X}(t) &= \frac{i}{\hbar}e^{i\hat{\mathcal{L}}^Q t}\left[\hat{H}, \hat{X}\right] = \frac{i}{\hbar}\left(\left[\hat{H}, \hat{X}\right]\right)(t), \end{aligned} \tag{2.35}$$

where $e^{i\hat{\mathcal{L}}^Q t}\hat{A} = e^{i\hat{H}t/\hbar}\hat{A}e^{-i\hat{H}t/\hbar}$. In the above equation, the time arguments outside the brackets indicate that one should first evaluate the commutator, then apply the time dependence. Taking the partial Wigner transform of the above equations, assuming that the subsystem and bath are initially decoupled, and retaining only zeroth order terms in $\hbar$ in the resulting Moyal product expansion, we obtain the

DECIDE equations of motion,

$$\begin{aligned}
\frac{d}{dt}(\hat{x}(t))_W &= \frac{i}{\hbar}\left(e^{i\hat{\mathcal{L}}^Q t}\right)_W e^{\hbar\Lambda/2i}\left(\left[\hat{H},\hat{x}\right]\right)_W \\
&\approx \frac{i}{\hbar}e^{i\hat{\mathcal{L}}^W t}\left(\left[\hat{H}_W,\hat{x}\right]\right) = \frac{i}{\hbar}\left(\left[\hat{H}_W,\hat{x}\right]\right)(t) \\
\frac{d}{dt}(\hat{X}(t))_W &\approx -e^{i\hat{\mathcal{L}}^W t}\left(\left\{\hat{H}_W,X\right\}_a\right) = -\left(\left\{\hat{H}_W,X\right\}_a\right)(t), \qquad (2.36)
\end{aligned}$$

where the antisymmetrized Poisson bracket is given by $\{\hat{H}_W,\hat{A}_W\}_a = \frac{1}{2}\{\hat{H}_W,\hat{A}_W\} - \frac{1}{2}\{\hat{A}_W,\hat{H}_W\}$. It should be noted that, to account for noncommutativity in the above equations, one has to replace coupling terms in the Hamiltonian with their Weyl-ordered symmetric forms, e.g., $\hat{x}X$ would be replaced by $\frac{1}{2}(\hat{x}X + X\hat{x})$. To arrive at Eq. 2.36, we assumed that $([\hat{H},\hat{x}])_W = [\hat{H}_W,\hat{x}]$ and $([\hat{H},\hat{X}])_W = -\frac{\hbar}{i}[\hat{H}_W,\hat{X}]_a$, i.e., the subsystem and bath are initially decoupled. Then, after expanding the exponential of the Poisson bracket operator Λ, we only kept the zeroth order term in $\hbar$, i.e.,

$$\left(e^{i\hat{\mathcal{L}}^Q t}\right)_W e^{\hbar\Lambda/2i}\left(\left[\hat{H},\hat{x}\right]\right)_W \approx e^{i\hat{\mathcal{L}}^W t}\left(\left[\hat{H}_W,\hat{x}\right]\right) = \left(\left[\hat{H}_W,\hat{x}\right]\right)(t). \qquad (2.37)$$

The errors caused by these approximations become significant when the subsystem dynamics is highly non-Markovian, namely when the dependence on the initial bath coordinates is important [24]. This can be the case for very low bath temperatures, very strong subsystem-bath coupling, and very slow baths, i.e., when memory effects are very pronounced [20, 24].

For the general form of the partially Wigner-transformed Hamiltonian given in

Eq. 2.33, the DECIDE equations of motion for the subsystem and bath DOF become

$$\begin{aligned}
\frac{d}{dt}\hat{x}(t) &= \frac{i}{\hbar}\left[\hat{H}_W, \hat{x}\right] = \frac{\hat{p}}{m}, \\
\frac{d}{dt}\hat{p}(t) &= \frac{i}{\hbar}\left[\hat{H}_W, \hat{p}\right] = -\frac{\partial \hat{V}_W}{\partial x}. \\
\frac{d}{dt}X(t) &= -\left\{\hat{H}_W, X\right\} = \frac{\partial \hat{H}_W}{\partial P}\cdot\frac{\partial X}{\partial X} - \frac{\partial \hat{H}_W}{\partial R}\cdot\frac{\partial X}{\partial P} = \frac{P}{m}, \\
\frac{d}{dt}P(t) &= -\left\{\hat{H}_W, P\right\} = -\frac{\partial \hat{V}_W}{\partial X}.
\end{aligned} \tag{2.38}$$

Finally, as in the case of the QCLE, one must select a convenient basis for the quantum subsystem to solve these equations.

To show that the total energy of system is conserved over the course of the dynamics, we start by taking the time derivative of a matrix element (in any basis) of the Hamiltonian

$$\frac{dH_W^{\alpha\alpha'}}{dt} = \left[\frac{\partial \hat{H}_W}{\partial \hat{x}}\frac{d\hat{x}}{dt} + \frac{\partial \hat{H}_W}{\partial \hat{p}}\frac{d\hat{p}}{dt} + \frac{\partial \hat{H}_W}{\partial X}\frac{dX}{dt} + \frac{\partial \hat{H}_W}{\partial P}\frac{dP}{dt}\right]^{\alpha\alpha'}, \tag{2.39}$$

where $H^{\alpha\alpha'} = \langle\alpha|\hat{H}_W|\alpha'\rangle$. Substituting the expressions for the time derivatives of the subsystem and bath DOFs in Eq. 2.38 into Eq. 2.39, we find that

$$\frac{dH_W^{\alpha\alpha'}}{dt} = 0, \tag{2.40}$$

thereby proving that the energy of the total system is conserved.

Chapter 3

DECIDE in the Position Basis

3.1 1D Proton Transfer Model

We first apply the DECIDE equations of motion in a position basis to simulating the dynamics of a simple 1D harmonic proton transfer model. This model represents a proton in a hydrogen bond.

3.1.1 Model

The Weyl-ordered Hamiltonian of our 1D harmonic proton transfer model is given by

$$\hat{H}_W = \frac{\hat{p}^2}{2m} + \frac{P^2}{2M} + A^0\hat{x}^2 + \frac{1}{2}k_1 X\hat{x} + \frac{1}{2}k_1\hat{x}X, \tag{3.1}$$

where $\hat{x}/\hat{p}$ is the position/momentum operator of the proton, X/P is the length/momentum of the hydrogen bond stretch, and A^0 and k_1 are constants. A sketch of the harmonic protonic potential is shown in Fig. 3.1. A convenient basis for representing a proton transfer problem is the set of quantum harmonic oscillator wave functions, i.e.,

$$\phi_n(x) = \langle x|\phi_n\rangle = (2^n n!\sqrt{\pi})^{-1/2} b^{1/2} H_n(bx)\exp[-b^2x^2/2], \tag{3.2}$$

where H_n is the n^{th} Hermite polynomial, b is an arbitrary constant, and $n = 0, 1, 2, \ldots$. Note that if X in Eq. 3.1 is 0, then the exact solution of the time-

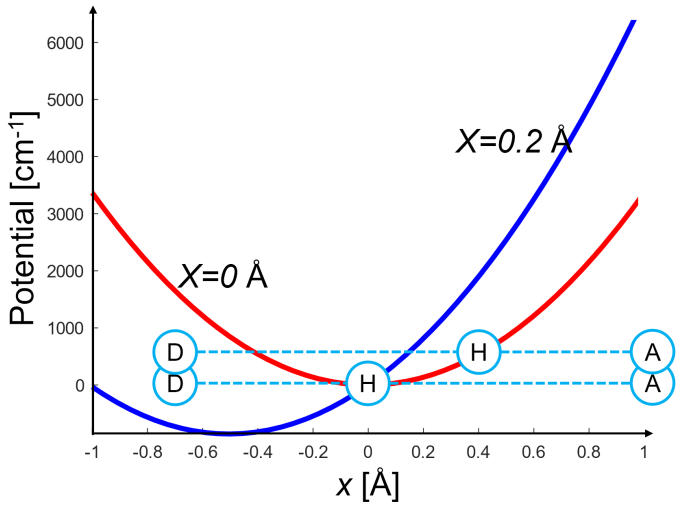

Figure 3.1: Harmonic potentials (red, $X = 0$ Å; blue, $X = 0.2$ Å) for a proton in a hydrogen bond, where D, H, and A represent the hydrogen bond donor, proton, and hydrogen bond acceptor, respectively. x and X correspond to the displacements of the proton and hydrogen bond length, respectively, from their equilibrium values.

independent Schrödinger equation is $\phi_n(x)$ with $b = \left(2mA^0/\hbar^2\right)^{1/4}$. In this work, we take $b = \left(8mA^0/\hbar^2\right)^{1/4}$ instead (for the reason given in Section 3.2). The eigenfunctions of $\hat{H}_W$ may be expanded in this basis as $|\psi_i\rangle = \sum_n c_n^i |\phi_n\rangle$, where c_n^i is the coefficient of the n^{th} basis function. For this expansion, we use 12 basis functions ($n = 0, \ldots, 11$). Substituting the eigenfunction expansion into the time-independent Schrödinger equation, we obtain an eigenvalue problem of the form $Hc = cE$, where H is the Hamiltonian matrix expressed in the chosen basis, c is a matrix containing the c_n^i's of the i^{th} eigenfunction, and E is a diagonal matrix containing the eigenvalues $E_i(X)$. The Hamiltonian matrix elements are calculated by numerical integration and the eigenvalue problem is solved (to obtain the c_n^i's and eigenvalues) using built-in functions in MATLAB. Using this method, we calculated the ground- and first-excited state adiabatic potential energy surfaces [$E_0(X)$ and $E_1(X)$, respectively] shown in Fig. 3.2.

The Schrödinger equation with the Hamiltonian in Eq. 3.1 can be solved analytically and exactly by first rewriting the potential energy as $A^0(x + \frac{k_1}{2A^0}Xx)^2 - \frac{k_1^2}{4A^0}X^2$.

The resulting adiabatic energies are

$$E_n(X) = \sqrt{\frac{2A^0}{m}}(n + \frac{1}{2})\hbar - \frac{k_1^2}{4A^0}X^2, \quad n = 0, 1, 2, 3, \ldots \tag{3.3}$$

where n labels the energy level. Comparing our variational result to the exact one, we find that good agreement is obtained when X is close to 0, but differences emerge when $|X| > 0.25$ (see Fig. 3.2). The convergence of the variational result can be improved by increasing the number of basis functions; however, the level of accuracy achieved with 12 basis functions is sufficient for our purposes.

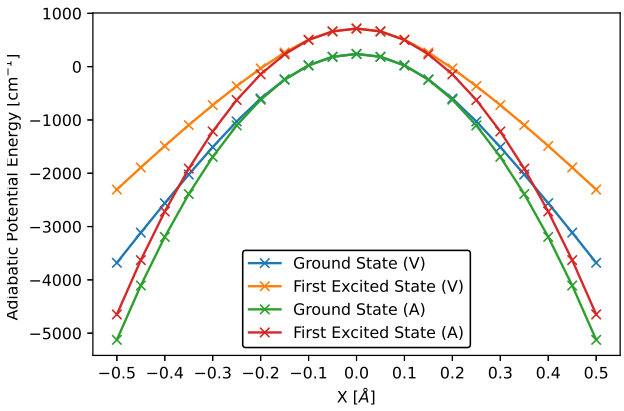

Figure 3.2: Ground- and first-excited state adiabatic potential energy surfaces of the 1D harmonic proton transfer model. V denotes a variational result and A denotes an analytical result. The following parameter values were used to obtain these surfaces: $A^0 = 3367.6$ cm^{-1} Å^{-2}, $k_1 = 1.7 \times 10^4$ cm^{-1} Å^{-2}, and $m = 1$ amu.

3.1.2 Simulation details

The DECIDE equations of motion for the harmonic proton transfer model are given by

$$\begin{aligned}
\frac{d}{dt}\hat{x}(t) &= \frac{i}{\hbar}[\hat{H}_W, \hat{x}] = \frac{\hat{p}}{m}, \\
\frac{d}{dt}\hat{p}(t) &= \frac{i}{\hbar}[\hat{H}_W, \hat{p}] = -A^0\hat{x} - k_1 X, \\
\frac{d}{dt}X(t) &= -\{\hat{H}_W, X\} = \frac{P}{m}, \\
\frac{d}{dt}P(t) &= -\{\hat{H}_W, P\} = -k_1\hat{x}.
\end{aligned} \tag{3.4}$$

In the harmonic oscillator basis, the equations of motion become

$$\begin{aligned}
\frac{d}{dt}x^{\alpha\alpha'}(t) &= \frac{p^{\alpha\alpha'}}{m}, \\
\frac{d}{dt}p^{\alpha\alpha'}(t) &= -A^0 x^{\alpha\alpha'} - k_1 X^{\alpha\alpha'}, \\
\frac{d}{dt}X^{\alpha\alpha'}(t) &= \frac{P^{\alpha\alpha'}}{m}, \\
\frac{d}{dt}P^{\alpha\alpha'}(t) &= -k_1 x^{\alpha\alpha'},
\end{aligned} \tag{3.5}$$

where, for example, $x^{\alpha\alpha'} = \langle\alpha|\hat{x}|\alpha'\rangle$ and $|\alpha\rangle$ is the α^{th} harmonic oscillator state. Given the size of the basis set, the total number of coupled differential equations is $12^2 \times 4$.

We assume the initial state of the composite system to be factorized, i.e., $\hat{\rho}(0) = \hat{\rho}_S(0)\rho_{B,W}(0)$, where $\hat{\rho}_S(0)$ is the initial density operator of the subsystem (viz., the proton) and $\rho_{B,W}(0)$ is the initial Wigner distribution of the bath (viz., the hydrogen bond stretch). In our simulations, the system is initialized in the adiabatic ground state $|\psi_0\rangle$ of the Hamiltonian in Eq. 3.1, such that $\hat{\rho}_S(t) = |\psi_0\rangle\langle\psi_0|$. In the harmonic oscillator basis, the initial values of the matrix elements of the subsystem degrees of

freedom $x^{\alpha\alpha'}$ and $p^{\alpha\alpha'}$ are given by the following analytical expressions:

$$\begin{aligned} x^{\alpha\alpha'}(0) &= \frac{1}{2}\left(\hbar^2/2mA^0\right)^{1/4}\left(\sqrt{\alpha+1}\delta_{\alpha+1,\alpha'}+\sqrt{\alpha'+1}\delta_{\alpha,\alpha'+1}\right), \\ p^{\alpha\alpha'}(0) &= i\left(2\hbar^2 mA^0\right)^{1/4}\left(\sqrt{\alpha+1}\delta_{\alpha+1,\alpha'}-\sqrt{\alpha'+1}\delta_{\alpha,\alpha'+1}\right). \end{aligned} \tag{3.6}$$

The initial values of the matrix elements of the bath degrees of freedom $X^{\alpha\alpha'}$ and $P^{\alpha\alpha'}$ are given by

$$X^{\alpha\alpha'}(0) = X_0\delta_{\alpha,\alpha'},\ P^{\alpha\alpha'}(0) = P_0\delta_{\alpha,\alpha'}, \tag{3.7}$$

where X_0/P_0 is the initial value of the bath position/momentum. In practice, X_0 and P_0 may be sampled from Wigner distributions corresponding to thermal equilibrium states. However, in this study, we choose $X(0) = -0.2$ Å (which is also used for the study in Section 3.2) and $P_0 = 50$ a.u., since we only generate a single trajectory for demonstration purposes. Starting from these initial conditions, the DECIDE equations of motion in Eq. 3.5 are integrated using the Runge Kutta 4th order method [38] with a time step of 1 a.u. to simulate the dynamics of the system.

The expectation value of a property $\hat{A}(t)$ may be calculated according to

$$\langle\hat{A}(t)\rangle = \sum_{\beta\beta'}\int \mathrm{d}X(0)\mathrm{d}P(0)\ A^{\beta\beta'}(t)\rho_S^{\beta'\beta}(0)\rho_{B,W}(0). \tag{3.8}$$

However, since we only consider single trajectories in this study, we take $\rho_{B,W}(0) = 1$. In particular, we are interested in the conservation of the total energy along a trajectory, which is calculated according to

$$\langle\hat{H}(t)\rangle = \sum_{\alpha\alpha'} H^{\alpha\alpha'}(t)\rho_S^{\alpha'\alpha}(0). \tag{3.9}$$

3.1.3 Results

Figure 3.3 shows the values of X, adiabatic energy, bath kinetic energy, and total energy along a representative trajectory. For a positive initial value of P_0, we see

that X increases up till about 4000 time steps and then starts to decrease. The adiabatic energy increases, while the bath kinetic energy decreases over the course of this trajectory. Finally, as seen in Fig. 3.3d, the total energy of the system is well-conserved along this trajectory.

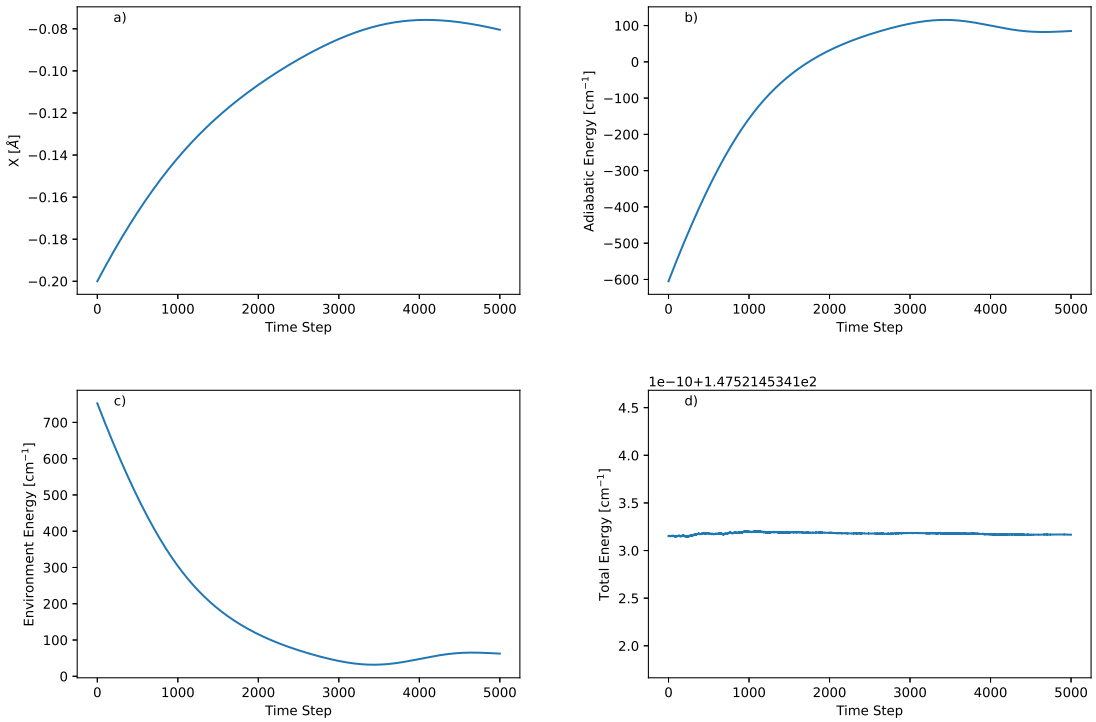

Figure 3.3: Results for the 1D harmonic proton transfer model obtained with a time step of 1 a.u. and the following parameter values: $A^0 = 3367.6$ cm^{-1} Å^{-2}, $k_1 = 1.7 \times 10^4$ cm^{-1} Å^{-2}, $m = 1$ amu, $M = 200$ amu, X_0 = -0.2 Å, and $P_0 = 50$ au. (a) Bath position, $X(t)$, (b) Adiabatic energy, $\langle \frac{\hat{p}^2}{2m} + A^0\hat{x}^2 + \frac{1}{2}k_1 X\hat{x} + \frac{1}{2}k_1\hat{x}X\rangle$, (c) Bath kinetic energy, $\frac{P^2}{2M}$, (d) Total system energy, $\langle \hat{H}\rangle(t)$.

3.2 2D Proton Transfer Model

3.2.1 Model

Next, we consider a simple 2D proton transfer model inspired by the well-known Azzouz-Borgis model [39], which was designed to describe the proton transfer dynamics in a hydrogen-bonded phenolamine complex dissolved in methyl chloride (see Fig. 3.4). Our goal is to test the ability of the DECIDE method to tackle a more realistic model of a proton transfer reaction in solution. This model, due to Jain and Subotnik [31], is composed of one protonic degree of freedom $\hat{x}$ (treated quantum mechanically), one hydrogen-bond donor-acceptor distance X_2 (treated classically), and one low-frequency solvent coordinate X_1 (treated classically). Its Hamiltonian is given by

$$\hat{H}_W = \frac{\hat{p}^2}{2m} + \frac{P_1^2}{2M_1} + \frac{P_2^2}{2M_2} + \hat{V}(\hat{x}, X_1, X_2), \tag{3.10}$$

where

$$V(\hat{x}, X_1, X_2) = V_0(\hat{x}) + V_1(X_1, X_2) + V_c(\hat{x}, X_1, X_2). \tag{3.11}$$

In the above equation,

$$V_0(\hat{x}) = A^0\hat{x}^2 + B^0\hat{x}^4, \tag{3.12}$$

$$V_1(X_1, X_2) = \frac{1}{2}M_1\omega_1^2X_1^2 + \frac{1}{2}M_2\omega_2^2X_2^2 + k_3X_1X_2 \tag{3.13}$$

and

$$V_c(\hat{x}, X_1, X_2) = \frac{1}{2}k_1\hat{x}X_1 + \frac{1}{2}k_1X\hat{x} + \frac{1}{2}k_2\hat{x}^2X_2 + \frac{1}{2}k_2X_2\hat{x}^2. \tag{3.14}$$

The protonic potential $V_0(\hat{x})$ is a double-well potential. We note that, if one expands $V_0(\hat{x})$ about a point $x_0 = \pm\sqrt{-\frac{A^0}{2B^0}}$ corresponding to the lowest energy, i.e.,

$$V_0(\hat{x} - x_0) = -\frac{A^{0\,2}}{4B^0} - 4A^0(\hat{x} - x_0)^2 + \ldots, \tag{3.15}$$

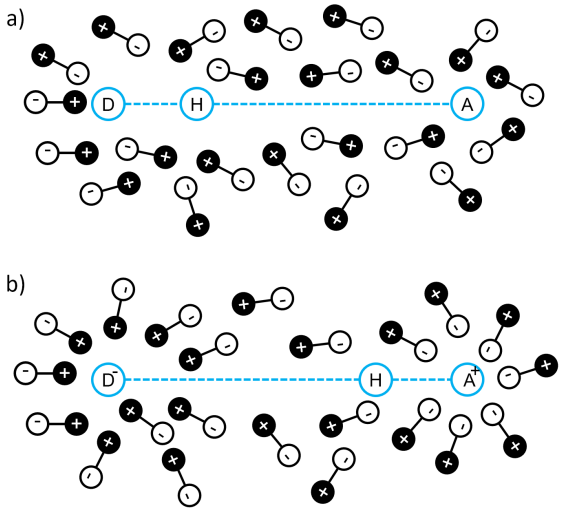

Figure 3.4: Proton transfer in a hydrogen-bonded complex (D-H-A) dissolved in a polar solvent. (a) Complex in the covalent state with the solvent unpolarized, and (b) complex in the ionic state with solvent polarized.

and neglects the terms of $\mathcal{O}(x^3)$ or higher, the time-independent Schrödinger equation could be solved analytically to yield the same solution as in Eq. 3.2 with x replaced by $x - x_0$.

Regarding the parameter values, we first used the values given in Ref. [31] in an effort to reproduce (at least qualitatively) some results in that study. However, after repeated attempts, we were not able to reproduce the results using the values as given. Instead, we found a new parameter set (except for the values of A_0 and B^0, which were the same as in Ref. [31]), which gave rise to very similar adiabatic potential energy surfaces to those in Fig. 7d of Ref. [31] (see Fig. 3.5). The details of how we arrived at the parameter values are provided in Appendix A.

3.2.2 Simulation details

Given the double-well character of the protonic potential, one may think to choose a non-orthogonal basis consisting of two sets of harmonic oscillator basis functions, each of which is centred at a different minimum of the potential. However, when con-

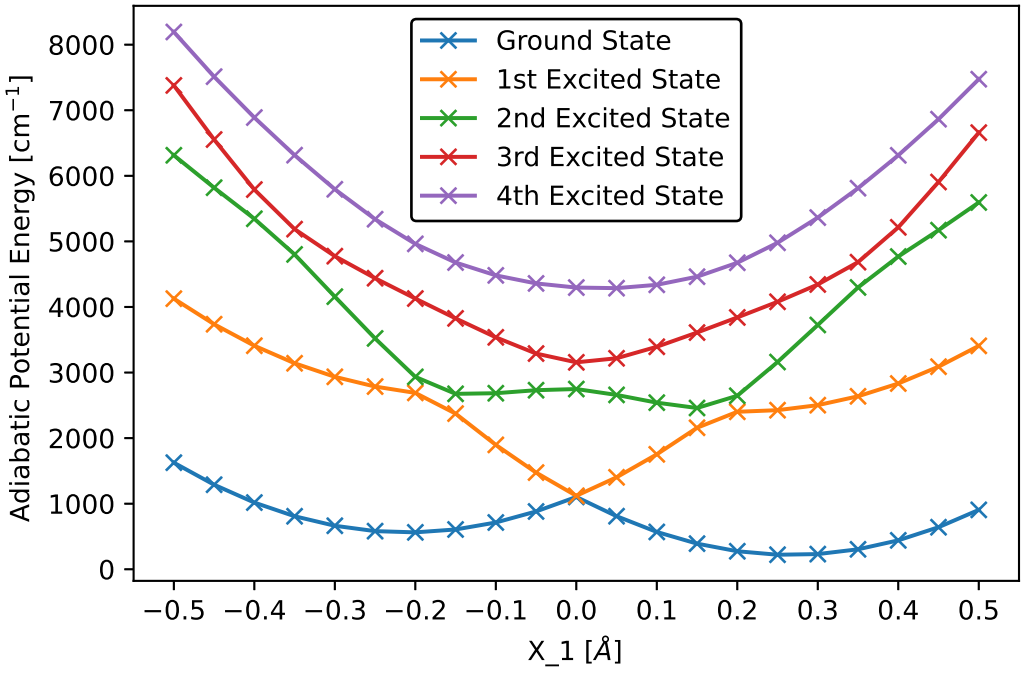

Figure 3.5: 1D slices along $X_2 = 0.18$ Å of the first five adiabatic potential energy surfaces $\langle\psi_n|\frac{\hat{p}^2}{2m} + V_0 + V_c|\psi_n\rangle + V_1$, generated with 16 harmonic oscillator basis functions.

sidering the sum of V_0 and V_c, it turns out that a single harmonic oscillator basis [as defined in Eq. 3.2 with $b = \left(8mA^0/\hbar^2\right)^{1/4}$] centered at $x = 0$ was more appropriate. This is due to the fact that the first order terms in Eq. 3.14 make the potential asymmetric and shift the minima significantly, making it difficult to choose appropriate centers for the two sets of basis functions. To solve the time-independent Schrödinger equation for this model, we use the same approach as described in Section 3.1. As in the case of the 1D proton transfer model, we use 12 harmonic oscillator basis functions to expand the adiabatic eigenfunctions.

In the harmonic oscillator basis, the $12^2 \times 6$ coupled DECIDE equations of motion

for this model are

$$
\begin{aligned}
\frac{d}{dt}x^{\alpha\alpha'}(t) &= \frac{i}{\hbar}[\hat{H}_W, \hat{x}]^{\alpha\alpha'} = \left[\frac{\hat{p}(t)}{m}\right]^{\alpha\alpha'}, \\
\frac{d}{dp}p^{\alpha\alpha'}(t) &= \frac{i}{\hbar}[\hat{H}_W, \hat{p}]^{\alpha\alpha'} = \left[-2A_0\hat{x}(t) - 4B_0(\hat{x}^3(t)) - k_1X_1(t) - k_2\hat{x}(t)X_2(t) - k_2X_2(t)\hat{x}(t)\right]^{\alpha\alpha'}, \\
\frac{d}{dt}X_1^{\alpha\alpha'}(t) &= -\{\hat{H}_W, X_1\}^{\alpha\alpha'} = \left[\frac{P_1(t)}{M}\right]^{\alpha\alpha'}, \\
\frac{d}{dt}X_2^{\alpha\alpha'}(t) &= -\{\hat{H}_W, X_2\}^{\alpha\alpha'} = \left[\frac{P_2(t)}{M}\right]^{\alpha\alpha'}, \\
\frac{d}{dt}P_1^{\alpha\alpha'}(t) &= -\{\hat{H}_W, P_1\}^{\alpha\alpha'} = \left[-M\omega_1^2X_1(t) - k_3X_2(t) - k_1\hat{x}(t)\right]^{\alpha\alpha'}, \\
\frac{d}{dt}P_2^{\alpha\alpha'}(t) &= -\{\hat{H}_W, P_2\}^{\alpha\alpha'} = \left[-M\omega_2^2X_2(t) - k_3X_2(t) - k_2\hat{x}^2(t)\right]^{\alpha\alpha'}. \qquad (3.16)
\end{aligned}
$$

To generate a trajectory, we choose the initial values of the bath coordinates to be $X_1 = -0.2$ Å, $X_2 = 0.1$ Å, $P_1 = 50$ au, and $P_2 = 50$ au. The subsystem is initialized in the ground state of the Hamiltonian in Eq. 3.10, with the same initial values of the quantum coordinates $x^{\alpha\alpha'}$ and $p^{\alpha\alpha'}$ as in Eq. 3.6. The equations of motion are integrated using the Runge Kutta 4th order method [38] with a time step of 1 a.u.

3.2.3 Results and discussion

We now present and discuss the results of a detailed analysis, which demonstrates the issues that can arise when using an incomplete basis set for this model. In Fig. 3.6a, we present the total energy, calculated using Eq. 3.1.2, along a representative trajectory. As can be seen, the total energy is not conserved. In Fig. 3.6b, we plot $X_2(t)$ vs. $X_1(t)$ over the course of this trajectory. Although the total energy is not conserved, this result is at least qualitatively correct at early times, since we expect the bath coordinates to move along positive directions when the initial momenta are both positive. When the size of the basis set is increased from 12 to 100 functions, we see that the total energy converges to a particular curve as a function of time, but remains not conserved (see Fig. 3.7). Similarly, increasing the size of the basis set

causes the trajectory of the bath coordinates X_1 and X_2 to converge to a particular curve. These results highlight an issue with casting the DECIDE equations for this model in a finite position basis, which we will discuss next.

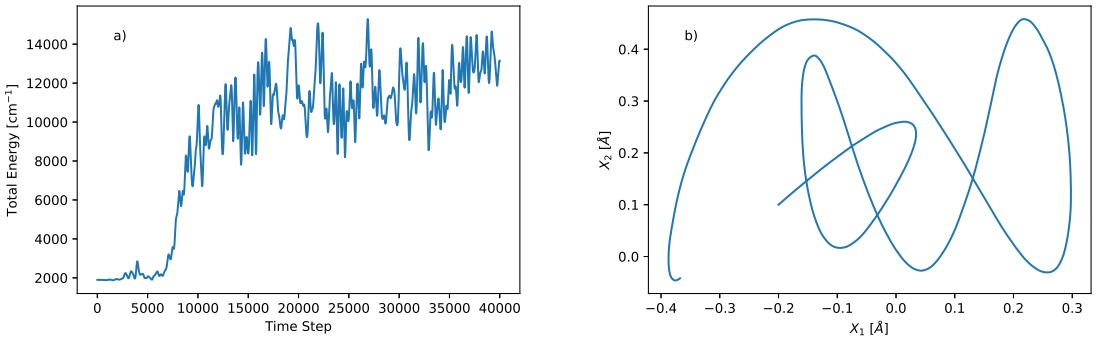

Figure 3.6: (a) Total energy $\langle \hat{H} \rangle$ vs. time along a representative trajectory, starting from $X_1(0)$ = -0.2 Å, $X_2(0)$ = 0.1 Å, and $P_1(0) = P_2(0) = 50$ au, and generated using a time step of 1 au, $m = 1$ amu, and $M = 200$ amu, (b) A plot of $X_1(t)$ vs. $X_2(t)$ over the course of this trajectory.

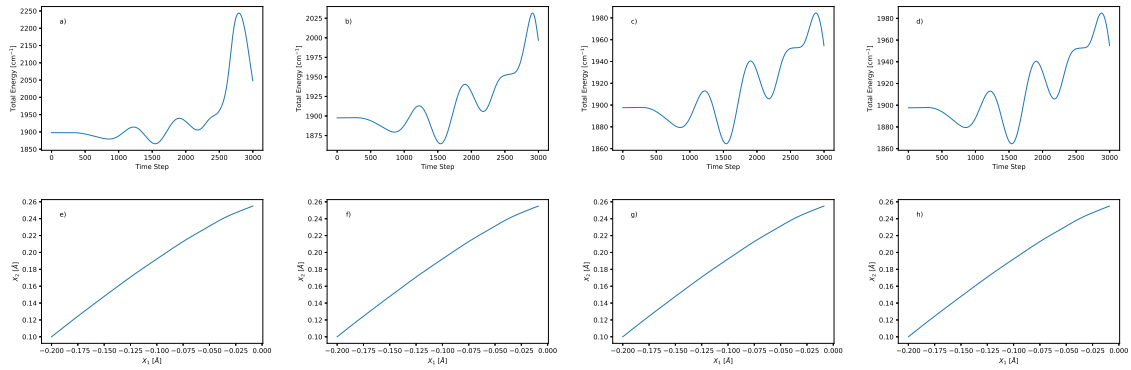

Figure 3.7: Effect of varying the number of basis functions on the total energy $\langle \hat{H} \rangle$: (a)12, (b) 20, (c) 50, and (d) 100 functions. Effect of varying the number of basis functions on the $X_1(t)$ vs. $X_2(t)$ plots: (e)12, (f) 20, (g) 50, and (h) 100 functions.

To gain insight into this issue, we first note that the matrix elements $(x^n)^{\alpha\alpha'}$ (for $n \geq 2$) are not evolved directly in the DECIDE method. Rather, the value of $(x^2)^{\alpha\alpha'}$,

for example, is calculated by first expanding it as follows,

$$(x^2)^{\alpha\alpha'} = \sum_{i=1}^{N} x^{\alpha i} x^{i\alpha'}, \tag{3.17}$$

where N is the number of basis functions. Alternatively, in matrix form, we may write

$$\begin{vmatrix} (x^2)^{11} & (x^2)^{12} & \dots & (x^2)^{1N} \\ (x^2)^{21} & (x^2)^{22} & \dots & (x^2)^{2N} \\ \dots & \dots & \dots & \dots \\ (x^2)^{N1} & (x^2)^{N2} & \dots & (x^2)^{NN} \end{vmatrix} = \begin{vmatrix} x^{11} & x^{12} & \dots & x^{1N} \\ x^{21} & x^{22} & \dots & x^{2N} \\ \dots & \dots & \dots & \dots \\ x^{N1} & x^{N2} & \dots & x^{NN} \end{vmatrix} \times \begin{vmatrix} x^{11} & x^{12} & \dots & x^{1N} \\ x^{21} & x^{22} & \dots & x^{2N} \\ \dots & \dots & \dots & \dots \\ x^{N1} & x^{N2} & \dots & x^{NN} \end{vmatrix} \tag{3.18}$$

For convenience, we use the forward Euler integration method to demonstrate the issue associated with representing the DECIDE equations of motion for this model in a finite position basis, i.e.,

$$f(t = \Delta t) = f(t = 0) + \frac{df}{dt}(t = 0)\Delta t, \tag{3.19}$$

where $f(x)$ is an arbitrary time-dependent function. To reduce the numerical error in the Euler method (since it is much less accurate than the Runge Kutta 4th order method), we choose a very small time step of $\Delta t = 0.025$ a.u. for this analysis. According to Eq. 3.6, for an infinitely large basis set, the values of the $x^{\alpha\alpha'}$ matrix

elements (in units of Bohr radius) at $t = 0$ are

$$\begin{vmatrix} 0 & 0.2513 & 0 & 0 & 0 & 0 & 0 & 0 & \dots \\ 0.2513 & 0 & 0.3554 & 0 & 0 & 0 & 0 & 0 & \dots \\ 0 & 0.3554 & 0 & 0.4353 & 0 & 0 & 0 & 0 & \dots \\ 0 & 0 & 0.4353 & 0 & 0.5027 & 0 & 0 & 0 & \dots \\ 0 & 0 & 0 & 0.5027 & 0 & 0.562 & 0 & 0 & \dots \\ 0 & 0 & 0 & 0 & 0.562 & 0 & 0.6156 & 0 & \dots \\ 0 & 0 & 0 & 0 & 0 & 0.6156 & 0 & 0.6649 & \dots \\ 0 & 0 & 0 & 0 & 0 & 0 & 0.6649 & 0 & \dots \\ 0 & 0 & 0 & 0 & 0 & 0 & 0 & 0.7109 & \dots \\ \vdots & \vdots & \vdots & \vdots & \vdots & \vdots & \vdots & \vdots & \ddots \end{vmatrix} .$$

As can be seen, this matrix is sparse, with non-zero elements only immediately above and below the diagonal elements. Let us now consider how to calculate at $t = 0$ an accurate value of $(x^3)^{9,10}$, for example, which can be expanded as follows,

$$\begin{aligned} (x^3)^{9,10} &= \sum_{i=1}^{\infty}\sum_{j=1}^{\infty} x^{9,i}x^{i,j}x^{j,10} \\ &= (x^{9,8}x^{8,9} + x^{9,10}x^{10,9})x^{9,10} + (x^{9,10}x^{10,11})x^{11,10}, \end{aligned} \tag{3.20}$$

where we have used the fact that the $x^{\alpha\alpha'}$ matrix at $t = 0$ is sparse to simplify the sums and arrive at the second line of the equation. In other words, to accurately evaluate $(x^3)^{9,10}$, one does not require an infinitely large basis set; instead, one may reliably evaluate the second line of Eq. 3.20 when $N = 12$. The same is true for $(x^3)^{10,11}$ at $t = 0$ when $N = 12$. On the other hand, if $N = 12$, the calculation for $(x^3)^{11,12}$ at $t = 0$ will not reliable, as the required evaluation of $x^{12,13}$ is not possible when the basis set contains only 12 functions.

According to Eq. 3.19, the value of each matrix element at a given time depends on its previous value. An unreliable evaluation of $(x^3)^{11,12}$ will make $\frac{d}{dt}p^{11,12}$ at $t = 0$ unreliable, which will make $p^{11,12}$ at $t = 0.025$ a.u. unreliable. Then, $x^{11,12}$ at $t = 0.05$ a.u. will become unreliable. Thus, the matrix element $(x^3)^{10,11}$ at $t = 0.05$ a.u. (whose

evaluation relies on $x^{11,12}$) becomes unreliable starting at $t = 0.05$ a.u. Based on this example, one can therefore expect that more matrix elements become unreliable as time evolves. Initially, only the edge elements of the $(x^3)^{\alpha\alpha'}$ matrix are unreliable, but as time goes on, the inner elements become unreliable too.

Another way to explain this is by considering the zero elements in the $x^{\alpha\alpha'}$. The first line of Eq. 3.20 is a summation over an infinite number of terms. One is able to simplify the sums because there are many zero elements in the initial matrix. If all $x^{\alpha\alpha'}$ matrix elements are non-zero, to evaluate $(x^3)^{9,10}$ we would have to evaluate terms like $x^{9,13}$, which are absent if $N = 12$. Although the initial matrix has zero elements, it can be verified that many elements will become non-zero after several steps, e.g. $x^{8,0} = 0$ at $t = 0$, but after four steps, it becomes non-zero. This deterioration process can be very fast due to the cubic terms in the DECIDE equations (see Eq. 3.16). For a basis set with 500 basis functions, it takes less than 30 time steps (0.75 a.u.) with the forward Euler integrator to make all elements unreliable, which is much shorter than any timescale of interest. It is these unreliable elements which ultimately lead to a breakdown in the energy conservation.

In the case of the 1D harmonic proton transfer model, the total energy is conserved because there are no x^2 or higher order terms in the equations of motion. That being said, there are still some small errors when calculating energies because there are x^2 and p^2 terms in the Hamiltonian (see Eq. 3.1).

Chapter 4

Enhancing the Performance of an Open Quantum Battery

4.1 Introduction

A quantum battery (QB) is a device that can store energy in a quantum system and release the energy when needed. In practice, a QB may interact with an environment (known as an open QB), which could lead to losses that negatively impact its performance. Thus, any theoretical studies of QBs should account for the presence of an environment. Along these lines, one can model an open QB as an open quantum network (OQN), which is composed of a network of quantum systems (known as *sites*) some or all of which are coupled to an environment that cause decoherence and dissipation processes to occur [40, 41, 42].

Over the years, researchers have proposed a number of ways for protecting a quantum system from its environment. One well-known approach is based on the concept of a decoherence-free subspace (DFS) − a subspace of the Hilbert space where only unitary dynamics takes place [43, 44]. As a result, this subspace is free from the influence of dissipation and decoherence by an environment. As has been proved in Refs. [45], [46], and [47], if there exists a unitary operator that commutes with all elements in the master equation, the system will possess *invariant*

subspaces. Among such subspaces, the one-dimensional subspaces are DFSs because the dynamics maps them onto themselves. A quantum state that lives in a DFS is a dark state (DS). DFSs and DSs have many potential applications in quantum information and quantum computing [48, 49, 50, 51, 52, 53]. Recently, researchers have proposed several ideas for stabilizing and enhancing the performance of QBs and other OQNs by utilizing DFSs [30, 54, 55, 56]. In Ref. [30], our group exploited the concept of a symmetry-protected dark state to propose a model for an open excitonic quantum battery (EQB) that is capable of storing an exciton for an indefinite period of time despite being coupled to thermal baths.

The effect of temperature gradients on energy/charge transport in nanoscale systems has been the subject of intensive study by both theorists and experimentalists over the past two decades. By introducing a temperature gap between two thermal baths connected to a quantum system, researchers have predicted and observed thermal rectification [57, 58], nonequilibrium heat transport [59, 20, 19], and mass flux [60, 61]. In our group's previous study [30], we simulated the exciton population dynamics of the EQB coupled to two baths with equal temperatures during the discharge phase, but did not study the population and energy transfer dynamics in the presence of a thermal gradient. Given the interesting nonequilibrium transport phenomena observed in other quantum systems, a study exploring the effects of different temperature gaps on the population/energy discharge dynamics is worthwhile. Thus, in this work, we study both the energy changes and populations dynamics of the open QB during the discharge phase, over a wide range of bath temperature gaps, bath reorganization energies, and site energies. Our goal is to find parameter regimes that maximize the performance of the battery in discharging both energy and exciton population.

4.2 QB Model

Following Ref. [30], we consider the same OQN model of a para-benzene-like molecule. Setting $\hbar = 1$, the Hamiltonian of the closed network is given by

$$\hat{H}_N = \sum_{n=1}^{6} E_n |n\rangle\langle n| + h \sum_{\langle n,m \rangle} |n\rangle\langle m|, \tag{4.1}$$

where $|n\rangle$ corresponds to a singly excited state [62, 63] localized on site n, E_n is the energy of site n, h is the nearest-neighbor electronic coupling strength, and the sum $\langle n, m\rangle$ denotes a cyclic summation over the nearest-neighbour sites in the network. The numbering of the sites is depicted in Figure 4.1. To construct the OQN, the two para-sites of the network are coupled to heat baths each containing a collection of harmonic oscillators. The sum of the bath Hamiltonians and network-bath coupling terms is given by

$$\hat{H}_B + \hat{H}_{NB} \;=\; \frac{1}{2} \sum_{n \in SSs} \sum_{j}^{M} \left[\hat{P}_{n,j}^2 + \omega_{n,j}^2 \left(\hat{R}_{n,j} - \frac{C_{n,j}}{\omega_{n,j}^2} |n\rangle\langle n| \right)^2 \right], \tag{4.2}$$

where M is the number of harmonic oscillators in each bath, $\hat{P}_{n,j}$ and $\hat{R}_{n,j}$ are the mass-weighted momentum and position operators of the jth oscillator, respectively, $\omega_{n,j}$ is the corresponding frequency, and $C_{n,j}$ is the bath-network coupling strength. The sites coupled to the baths are referred to as surface sites (SSs) while the remaining sites are referred to as bulk sites (BSs). In contrast to the case in Hückel theory where $E_n = \varepsilon$ for all n , we choose the same E_n values for the BSs but different values for the SSs.

Despite the different SS energies and attached baths, the system possesses the following unitary symmetry operator [64]

$$\hat{\Pi} \;=\; |1\rangle\langle 1| + |4\rangle\langle 4| + |2\rangle\langle 6| + |3\rangle\langle 5| + h.c., \tag{4.3}$$

which satisfies

$$[\hat{\Pi}, \hat{H}_N] = 0, \quad [\hat{\Pi}, |n\rangle\langle n|] = 0 \quad \forall n \in \text{SSs}. \tag{4.4}$$

As a result, $\hat{\Pi}$ shares the same eigenstates with $\hat{H}_N$. Due to the existence of this symmetry operator, the system possesses two DFSs with the corresponding DSs $|\psi_\alpha\rangle$ and eigenvalues u_α [46, 65]

$$\begin{aligned} |\psi_1\rangle &= \frac{1}{2}\left(|5\rangle + |6\rangle - |2\rangle - |3\rangle\right), \quad u_1 = E_{BS} + h \\ |\psi_2\rangle &= \frac{1}{2}\left(|3\rangle + |6\rangle - |2\rangle - |5\rangle\right), \quad u_2 = E_{BS} - h \end{aligned} \tag{4.5}$$

where E_{BS} denotes the site energy (E_n) of the BSs. If the system is initialized in the dark state $|\psi_\alpha\rangle$, it will undergo a dissipationless dynamics, i.e., if we define the population of each site in terms of the projection operator $\hat{\mathcal{P}}_{nn} = |n\rangle\langle n|$, then the dark state will be invariant under the effect of the evolution operator of the composite system and the site populations will be

$$\langle \hat{\mathcal{P}}_{nn}(t)\rangle = \langle \hat{\mathcal{P}}_{nn}(0)\rangle = \begin{cases} 0, & \forall n \in \text{SSs} \\ \frac{1}{4}, & \forall n \in \text{BSs}, \end{cases} \tag{4.6}$$

where $\langle\cdot\rangle$ denotes an ensemble average. Because the excitation is stored indefinitely in this state, this is termed the *storage phase*.

When a symmetry-breaking perturbation (SBP) is added to the OQN, the symmetry operator and DSs no longer exist and the QB may begin to discharge a stored exciton. In this study, this is done by attaching a bath of M harmonic oscillators to sites 2 and 3 simultaneously [65]. The corresponding Hamiltonian for the SBP and network-SBP coupling is

$$\hat{H}_P + \hat{H}_{NP} = \frac{1}{2}\sum_k^M \left[\hat{p}_k^2 + \Omega_k^2\left(\hat{r}_k - \frac{\gamma_k}{\Omega_k^2}\hat{S}\right)^2\right], \tag{4.7}$$

where $\hat{p}_k$, $\hat{r}_k$, Ω_k, and γ_k are the momentum operator, position operator, frequency, and coupling strength of the kth oscillator, respectively, and $\hat{S} = |2\rangle\langle 2| + |3\rangle\langle 3|$. This

phase is termed the *discharge phase*.

4.3 Simulation Details

Due to the large number of degrees of freedom (DOF) in the QB, thermal baths, and SBP, a fully quantum dynamical simulation of the composite system would be computationally expensive. Thus, following Ref. [30], we use a mixed quantum-classical method known as "Deterministic evolution of coordinates with initial decoupled equations" (DECIDE) [24], which treats the OQN quantum mechanically and the bath classically. Previously, the DECIDE method has been successfully applied to a host of model systems over a large range of parameter regimes [24, 20, 19, 28] and is thus expected to produce reliable results in this case. That being said, DECIDE may yield inaccurate results for systems with very slow heat baths (i.e., when the bath cut-off frequency is much smaller than the subsystem energy gaps) or with very low bath temperatures (neither of which is the case for the present model).

To apply the DECIDE method, we must first apply the partial Wigner transform [32, 2] to the classical DOF, viz., the positions and momenta of the bath and SBP oscillators. The partially Wigner-transformed Hamiltonian of the composite system is

$$\hat{H}_W \;=\; \hat{H}_N + \hat{H}_{NB}(\{R_{n,j}\}) + H_B(\{P_{n,j}\},\{R_{n,j}\}) + \chi\left[H_P(\{p_k\},\{r_k\}) + \hat{H}_{NP}(\{r_k\})\right], \tag{4.8}$$

where $P_{n,j}$, $R_{n,j}$, p_k, and r_k are the momentum and position variables of the baths and SBP. The parameter χ is equal to 1 when a SBP is attached to the OQN and 0 otherwise. The quantum coordinates of the OQN are taken to be $\hat{\mathcal{P}}_{nm} = |n\rangle\langle m|$, while the classical coordinates are the momenta and positions of the baths and SBP. According to the DECIDE method, the equations of motion for the quantum and

classical coordinates are given by [30]

$$
\begin{aligned}
\frac{d}{dt}\mathcal{P}^{\beta\beta'}_{nm}(t) &= i\left[\sum_{l=1}^{6} V_{ln}\hat{\mathcal{P}}_{lm}(t) - \sum_{v=1}^{6} V_{mv}\hat{\mathcal{P}}_{nv}(t)\right]^{\beta\beta'} \\
&\quad -\frac{i}{2}\sum_{j} C_{n,j}(R_{n,j}(t)\hat{\mathcal{P}}_{nm}(t) + \hat{\mathcal{P}}_{nm}(t)R_{n,j}(t))^{\beta\beta'}(\delta_{n,1}+\delta_{n,4}) \\
&\quad +\frac{i}{2}\sum_{j} C_{m,j}(R_{m,j}(t)\hat{\mathcal{P}}_{nm}(t) + \hat{\mathcal{P}}_{nm}(t)R_{m,j}(t))^{\beta\beta'}(\delta_{m,1}+\delta_{m,4}) \\
&\quad -\chi\frac{i}{2}\sum_{k} C_{k}(R_{k}(t)\hat{\mathcal{P}}_{nm}(t) + \hat{\mathcal{P}}_{nm}(t)R_{k}(t))^{\beta\beta'}(\delta_{n,2}+\delta_{n,3}) \\
&\quad +\chi\frac{i}{2}\sum_{k} C_{k}(R_{k}(t)\hat{\mathcal{P}}_{nm}(t) + \hat{\mathcal{P}}_{nm}(t)R_{k}(t))^{\beta\beta'}(\delta_{m,2}+\delta_{m,3}), \\
\frac{d}{dt}R^{\beta\beta'}_{n,j}(t) &= P^{\beta\beta'}_{n,j}(t), \\
\frac{d}{dt}P^{\beta\beta'}_{n,j}(t) &= -\omega^2_{n,j}R^{\beta\beta'}_{n,j}(t) + C_{n,j}\mathcal{P}^{\beta\beta'}_{nn}(t)(\delta_{n,1}+\delta_{n,4}), \\
\frac{d}{dt}r^{\beta\beta'}_{k}(t) &= p^{\beta\beta'}_{k}(t), \\
\frac{d}{dt}p^{\beta\beta'}_{k}(t) &= -\Omega^2_k r^{\beta\beta'}_{k}(t) + \chi\gamma_k(\hat{\mathcal{P}}_{22}+\hat{\mathcal{P}}_{33})^{\beta\beta'}(t),
\end{aligned}
\tag{4.9}
$$

where $V_{nn} = E_n + \sum_{j=1}^{M} C^2_{n,j}/(2\omega^2_{n,j})(\delta_{n,1}+\delta_{n,4}) + \chi\sum_{k=1}^{M}\gamma^2_k/(2\Omega^2_k)(\delta_{n,2}+\delta_{n,3})$ and $V_{nm} = h$. We assume the initial state of the system to be a factorized, i.e., $\hat{\rho}_{tot}(0) = \hat{\rho}_N(0)\rho_{B,W}(0)\rho_{P,W}(0)$, where $\hat{\rho}_N(0)$ is the initial density operator of the network, and $\rho_{B,W}(0)$ and $\rho_{P,W}(0)$ are the initial Wigner-transformed densities of the heat baths and SBP, respectively (N.B.: $\rho_{P,W}(0)$ is omitted when the OQN is not attached to the SBP). The initial state of the network is taken to be the dark state $\hat{\rho}_N(0) = |\psi_1\rangle\langle\psi_1|$, where $|\psi_1\rangle$ is defined in Eq. 4.5. The initial values of the quantum coordinates are always taken to be $\mathcal{P}^{\beta\beta'}_{nm} = \delta_{\beta,n}\delta_{m,\beta'}$. The bath oscillators are initialized in thermal

equilibrium states given by (setting $k_B = 1$)[34, 37]

$$\rho_{B,W}(0) = \prod_{n=1,4}\prod_{j=1}^{M} \frac{\tanh(\beta\omega_{n,j}/2)}{\pi} \times \exp\left[-\frac{2\tanh(\beta\omega_{n,j}/2)}{\omega_{n,j}}\left(\frac{P_{n,j}^2}{2} + \frac{\omega_{n,j}^2 R_{n,j}^2}{2}\right)\right], \tag{4.10}$$

where $\beta = 1/k_B T$ is the inverse temperature. The oscillators of the SBP are also initialized in a thermal equilibrium state with an analogous form to that of the baths. The initial positions and momenta of the bath and SBP oscillators are sampled from Eq. 4.10 and its analog for the SBP, respectively. The system-bath and system-SBP couplings are characterized by a Debye-Drude spectral density, i.e., $J(\omega_{n,j}) = 2\lambda_b \frac{\omega_{n,j}}{\omega_{n,j}^2+1}$. In this work, the spectral density is discretized to yield the following expressions for the coupling strengths $C_{n,j}$ and frequencies $\omega_{n,j}$ in Eq. 4.2 [66, 67]

$$\omega_{n,j} = \tan(j \arctan(\omega_{max}/\omega_c)/M)\omega_c, \tag{4.11}$$

$$C_{n,j} \;=\; 2\sqrt{\lambda_b \arctan(\omega_{max}/\omega_c)/(\pi M)}\,\omega_{n,j}, \tag{4.12}$$

where λ_b is the bath reorganization energy and ω_c is the bath cut-off frequency [68]. Previously, the 4th order Runge-Kutta method was used to integrate the DECIDE equations of motion in Eq. 4.9, yielding conserved total populations for the system under study [24, 30]. However, in this work, we found that a much smaller time step or a higher order integrator is needed for energy conservation and more accurate calculations of the various components of the total energy. High-order Runge-Kutta methods such as the 8th order method [69] can yield accurate results with a relatively large time step, but it contains many integration stages which increases the simulation time drastically. Considering the trade-off between the time step and number of integration steps, we employed the 6th order Runge-Kutta method in this work. For a 1 ps trajectory generated using this integrator with a time step of 0.16 fs, the total energy drift is less than 1×10^{-2} cm^{-1} (see Fig. B.1 in Appendix B).

The time-dependent populations of each site are calculated via ensemble averages

of the projection operators $\hat{P}_{nn}$, viz.,

$$\langle \hat{\mathcal{P}}_{nn}(t) \rangle = \sum_{\beta\beta'} \int d\boldsymbol{X}(0) \mathcal{P}_{nn}^{\beta\beta'}(t) \rho_N^{\beta'\beta}(0) \rho_{E,W}(0). \tag{4.13}$$

Similarly, the average total energy of the composite system is

$$\langle E_{tot}(t) \rangle = \sum_{\beta\beta'} \int d\boldsymbol{X}(0) \hat{H}_W^{\beta\beta'}(t) \rho_N^{\beta'\beta}(0) \rho_{E,W}(0). \tag{4.14}$$

In the above equations, $\rho_{E,W} = \rho_{B,W}$ in the absence of the SBP and $\rho_{E,W} = \rho_{B,W}\rho_{P,W}$ when the SBP is attached to the system. We have verified that $\sum_{n=1}^{6} \langle \hat{\mathcal{P}}_{nn}(t) \rangle = 1$ (i.e., population conservation) and $\frac{d}{dt} E_{tot}(t) = 0$ (i.e., energy conservation). The total energy of the composite system can be split into several parts: the energy of the OQN (E_N), the energy of the baths ($E_{NB} + E_B$), and the energy of the SBP ($E_{NP} + E_P$). E_N can be further split into the on-site energy and exchange energy, corresponding to the terms $\sum_{n=1}^{6} E_n |n\rangle\langle n|$ and $h \sum_{\langle n,m \rangle} |n\rangle\langle m|$, respectively, in the Hamiltonian in Eq. 4.1. All simulation results are averaged over 10,000 trajectories, which ensures that the error bars are much smaller than the symbols in the figures.

4.4 Results

We start by considering the time-dependent site populations and energies of the OQN, SBP, and baths in the storage ($\chi = 0$) and discharge ($\chi = 1$) phases, using the parameter values from Ref. [30], viz., $E_1 = 250$ cm^{-1}, $E_{i\in\{2,3,5,6\}} = 200$ cm^{-1}, $E_4 = 0$ cm^{-1} (N.B.: E_4 is smaller than the energies of the remaining sites because site 4 is set to be the exit site, which, in practice, would be attached to a sink that captures the exciton/energy), $h = 60$ cm^{-1}, $T_L = T_R = 300$ K, $T_p = 300$ K, $\lambda_b = 35$ cm^{-1}, $\lambda_p = 10$ cm^{-1}, $\omega_c = \omega_p = 106$ cm^{-1}, $\omega_{max} = 50\omega_c$, and $M = 100$. In Fig. 4.1a, we see that the populations of all sites are perfectly conserved during the storage phase (viz., the populations of sites 2, 3, 5, and 6 remain 0.25, and the populations of sites 1 and 4 remain 0). Similarly, as seen in Fig. 4.1c, the system, left bath, and

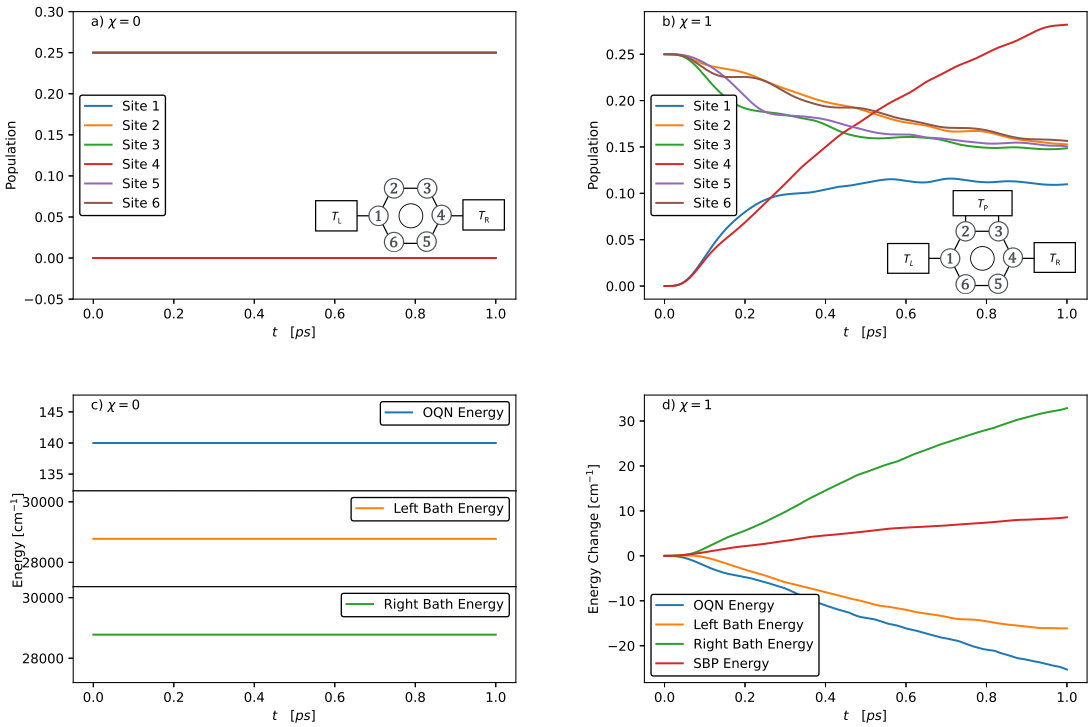

Figure 4.1: Time-dependent site populations (upper panels) and energies (lower panels) of the OQN, SBP, and baths in the storage (left panels) and discharge (right panels) phases. In panel d), energy changes are calculated by subtracting the initial value of the energy from the value at each time. The results were generated using the following parameter set: $E_1 = 250$ cm^{-1}, $E_{i\in\{2,3,5,6\}} = 200$ cm^{-1}, $E_4 = 0$ cm^{-1}, $h = 60$ cm^{-1}, $T_L = T_R = 300$ K, $T_p = 300$ K, $\lambda_b = 35$ cm^{-1}, $\lambda_p = 10$ cm^{-1}, $\omega_c = \omega_p = 106$ cm^{-1}, $\omega_{max} = 50\omega_c$, and $M = 100$.

right bath energies are perfectly conserved. Consistent with the theory, there is no population/energy leakage during the storage phase.

As seen in Fig. 4.1b, after attaching the SBP, the populations of sites 1 and 4 increase while the remaining site populations decrease over the 1 ps time period. At $t = 1$ ps, the population of site 4 (i.e., the exit site) is greater than that of site 1 and the BSs. In Fig. 4.1d, we plot the changes in the system (OQN), left bath, right bath, and SBP energies with respect to their initial values. As can be seen, the system and left bath energies decrease while the SBP and right bath energies increase. Thus, during the discharge phase, energy flows from the OQN and left bath into the right bath and SBP, with considerably more energy flowing to the right bath than to the SBP.

We now investigate the effects of varying the bath temperatures, bath reorganization energy, and site energies on the site populations and energy flow in the battery, in an effort to find parameter sets that will maximize the population of the exit site and minimize the energy loss of the OQN. To simplify our exploration of the parameter space, we vary one parameter at a time while keeping the remaining parameters fixed. First, we fix the temperature of the left bath at 300 K and vary the temperature of the right bath, while keeping the OQN, SBP, and remaining bath parameters unchanged. In Figures 4.2a and c, we see that increasing the right bath temperature leads to a decrease in the population of site 4 and relatively small increases in the populations of the remaining sites. As for the energy changes (see Figures 4.2b and d), the system and left bath lose energy, but the energy loss becomes smaller and remains relatively constant, respectively, with increasing right bath temperature. On the other hand, the SBP and right bath gain energy, but the amount of energy gain becomes smaller and remains relatively constant, respectively, with increasing right bath temperature. When we fix the temperature of the right bath at 300 K and vary the temperature of the left bath, the behaviours of the site populations are similar to those observed in the case when the temperature of the right bath is varied, except for that of site 4 which now exhibits a substantially smaller decrease (see Figure 4.2c). As for the energy changes (see Figure 4.2d), the behaviours of the SBP and OQN energies are similar to those observed in the case when the temperature of the right

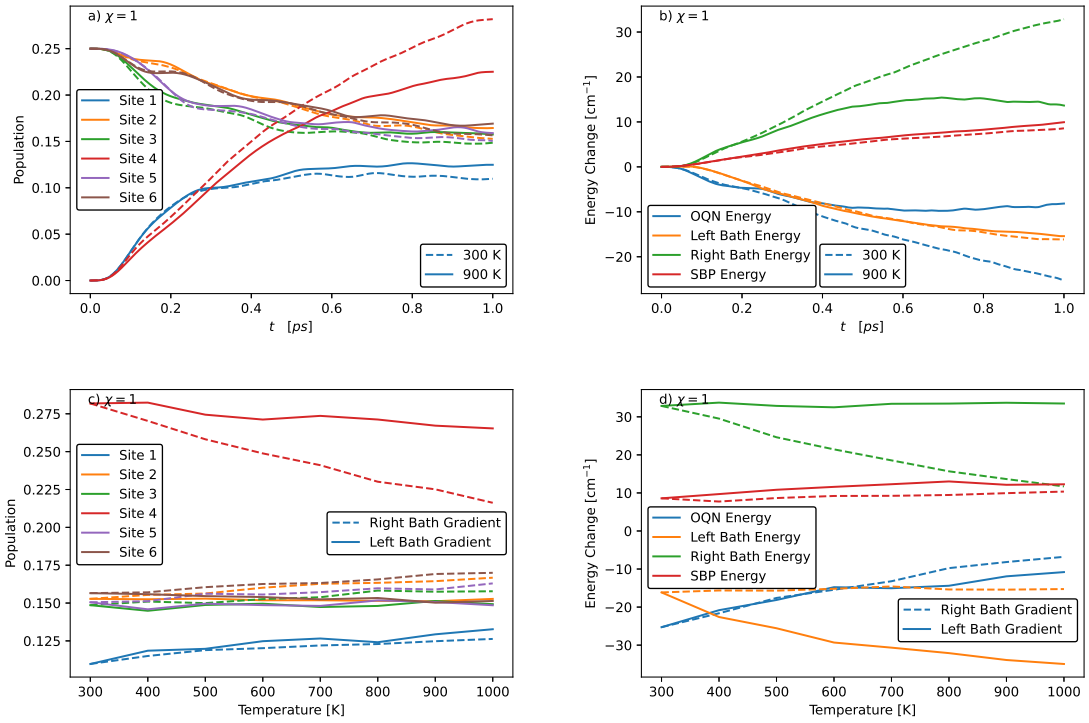

Figure 4.2: Site populations (left panels) and energy changes (right panels) in the discharge ($\chi = 1$) phase for different bath temperature gradients. (a-b) Time-dependent site populations and energy changes for right bath temperatures of 300 K (solid lines) and 900 K (dashed lines), with $T_L = 300$ K. (c-d) Site populations and energy changes after 1 ps for different right bath temperatures and a left bath temperature of 300 K (denoted by right bath gradient), and different left bath temperatures and a right bath temperature of 300 K (denoted by left bath gradient).

bath is varied. On the other hand, the bath energies are significantly different, with the energy changes of the left and right baths becoming more negative and remaining relatively constant, respectively, with increasing left bath temperature.

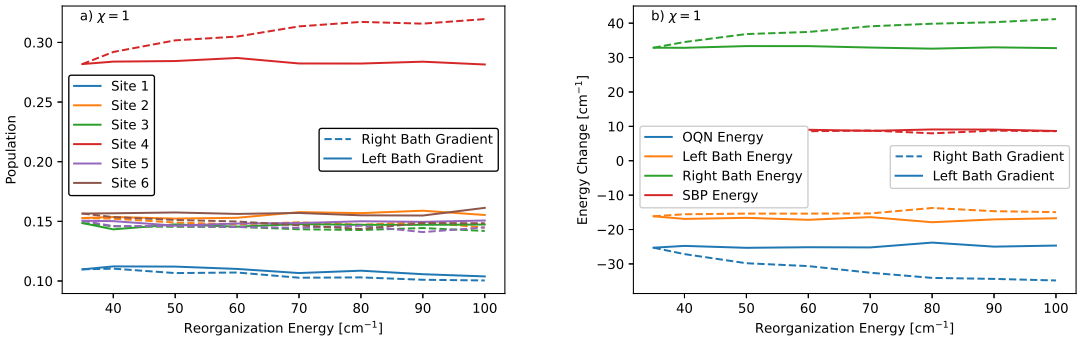

Figure 4.3: (a) Site populations and (b) energy changes in the discharge phase after 1 ps for different right bath reorganization energies and a left bath reorganization energy of 35 cm^{-1} (denoted by right bath gradient), and different left bath reorganization energies and a right bath reorganization energy of 35 cm^{-1} (denoted by left bath gradient).

Next, we vary the bath reorganization energy λ_b. From Fig. 4.3, we see that increasing the right bath reorganization energy causes the site 1/4 population to decrease/increase, the right bath energy to increase, and the system to lose more energy; the populations of the remaining sites, left bath energy, and SBP energy remain relatively constant. On the other hand, we see that increasing the left bath reorganization energy does not have a significant impact on the site population and energy changes.

We now investigate the effects of varying the SS energies on the site populations and energy changes. Results after 1 ps and time-dependent results for different combinations of the SS energies are given in Appendix B and Fig. 4.4, respectively. As seen in Fig. 4.4a, setting the SS energies equal to each other leads to roughly equal SS populations, with the SS populations decreasing when increasing from $E_1 = E_4 = 100$ cm^{-1} to $E_1 = E_4 = 250$ cm^{-1}. When the energies of the SSs are greater than those of the BSs, the BSs are more populated than the SSs after 1 ps. Conversely, when the

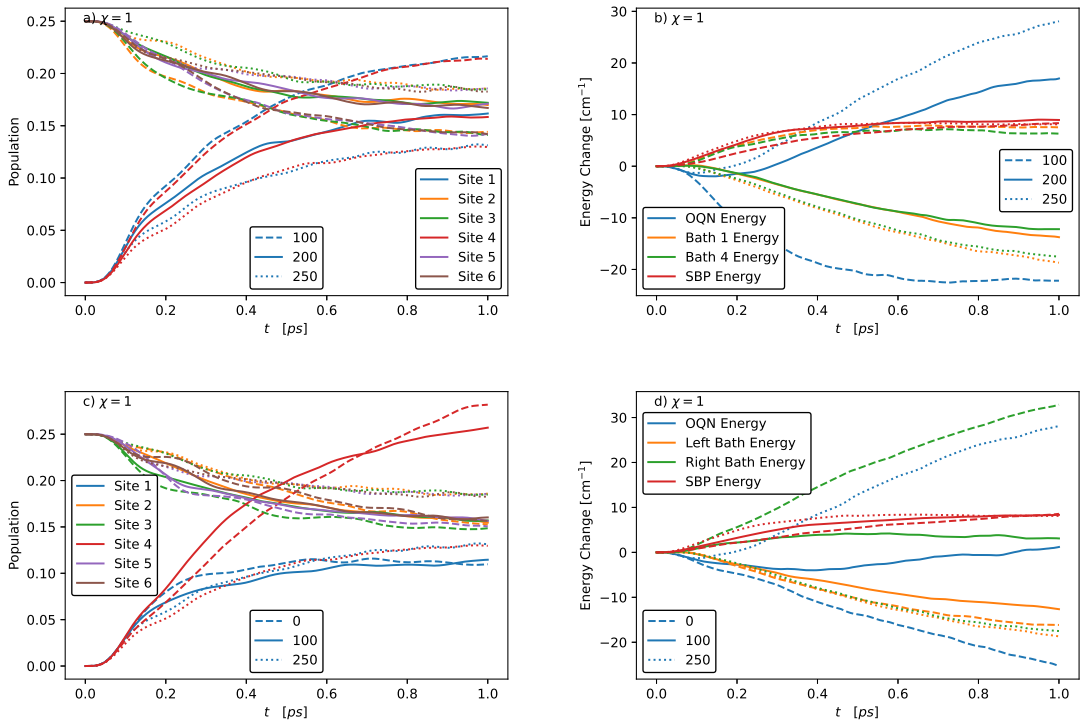

Figure 4.4: Time-dependent site populations (left panels) and energy changes (right panels) in the discharge phase ($\chi = 1$) for different SS energies. (a-b) Results for $E_1 = E_4 = 100$ cm^{-1}, $E_1 = E_4 = 200$ cm^{-1}, and $E_1 = E_4 = 250$ cm^{-1}. (c-d) Results for $E_1 = 250$ cm^{-1}, and $E_4 = 0$, 100, and 250 cm^{-1}. The values of the remaining parameters are $E_{i\in\{2,3,5,6\}} = 200$ cm^{-1}, $T_A = T_B = 300$ K, and $\lambda_b = 35$ cm^{-1}.

energies of the SSs are smaller than those of the BSs, the SSs are more populated than the BSs after 1 ps. When the energies of the SSs are equal to those of the BSs, we see that the SS and BS populations approach each other over time, becoming almost equal after 1 ps. With regards to the energy changes, setting the SS energies equal to each other leads to roughly equal changes in the left and right bath energies, with the bath energy changes decreasing and becoming more negative when increasing from $E_1 = E_4 = 100$ cm^{-1} to $E_1 = E_4 = 250$ cm^{-1}. More specifically, there are energy gains in the baths for $E_1 = E_4 = 100$ cm^{-1} and energy losses for the larger SS energies, with the loss increasing with increasing SS energy. Conversely, there

is an energy loss from the system when $E_1 = E_4 = 100$ cm^{-1} and energy gains for the larger SS energies, with the gain increasing with increasing SS energy. The SBP energy remains almost unchanged for the different SS energies. In Figs. 4.4c and d, we plot the results for $E_1 = 250$ cm^{-1} and different values of E_4. As can be seen, increasing the energy of site 4 from 0 to 100 cm^{-1} does not cause a significant change in the site 4 population; however, increasing the energy of site 4 from 100 to 250 cm^{-1} causes a $\approx 50\%$ drop in the site 4 population after 1 ps. Moreover, when the energy of site 4 is smaller than those of the remaining sites, site 4 becomes the most populated site after 1 ps. The populations of the remaining sights do not change significantly in going from $E_4 = 0$ to 100 cm^{-1}, but they each increase by several percent after 1 ps in going from $E_4 = 100$ to 250 cm^{-1}. As for the energy changes, increasing the energy of site 4 leads to more energy transfer from the right bath to the system, which in turn causes the system's energy to change from decreasing to increasing.

4.5 Discussion

4.5.1 Storage phase

As mentioned in the previous section, the OQN perfectly preserves the excitation during the storage phase. Because the initial values of $\langle\hat{\mathcal{P}}_{11}\rangle$ and $\langle\hat{\mathcal{P}}_{44}\rangle$ are zero, the expectation values of the coupling terms in the equations of motion (Eq. 4.9) are also zero (i.e., $\langle\sum_j C_{n,j}(R_{n,j}(t)\hat{\mathcal{P}}_{nm}(t) + \hat{\mathcal{P}}_{nm}(t)R_{n,j}(t))\rangle = 0$), causing $\frac{d}{dt}\langle\hat{\mathcal{P}}_{nn}(t)\rangle$ to remain zero for all times. Thus, there are no population changes during the storage phase.

In terms of the energies, we first consider the time derivatives of the bath energy matrix elements,

$$\frac{d}{dt}[H_B + \hat{H}_{NB}]^{\beta\beta'} = \frac{1}{2}\sum_j \left[\frac{C_{n,j}^2}{\omega_{n,j}^2}\frac{d}{dt}\hat{\mathcal{P}}_{nn} - C_{n,j}R_{n,j}\frac{d}{dt}\hat{\mathcal{P}}_{nn} - C_{n,j}\left(\frac{d}{dt}\hat{\mathcal{P}}_{nn}\right)R_{n,j}\right]^{\beta\beta'}, \tag{4.15}$$

where n on the RHS of the equation could either be 1 or 4, depending on whether the left bath or right bath is considered. The details of how we arrived at this equation are provided in Appendix B. We can see that the time derivative of the expectation value of the bath energy, $\frac{d}{dt}\langle H_B + \hat{H}_{NB}\rangle$, is 0 because $\frac{d}{dt}\mathcal{P}_{11}$ and $\frac{d}{dt}\mathcal{P}_{44}$ are 0. This indicates that there is no energy transfer between the bath and OQN during the storage phase, regardless of the parameter values (even if a thermal gradient between the baths is present). On the other hand, $\frac{d}{dt}\langle\sum_j^M P_{n,j}^2\rangle$ and $\frac{d}{dt}\langle\sum_j^M \omega_{n,j}^2 R_{n,j}^2\rangle$ are non-zero, which leads to an energy exchange between the kinetic and potential energies of the baths.

4.5.2 Discharge phase

After attaching the SBP to the OQN, the expectation values of the coupling terms appearing in the equations of motion (Eq. 4.9), viz., $\langle\sum_j C_{n,j}(R_{n,j}(t)\hat{\mathcal{P}}_{nm}(t)+\hat{\mathcal{P}}_{nm}(t)R_{n,j}(t))\rangle$, become non-zero. As a result, $\langle\hat{\mathcal{P}}_{nn}(t)\rangle$ and the energies start to change. As proposed in Section 4.3, the OQN energy can be written as the sum of on-site and exchange energies. The change in the exchange energy is given by

$$\Delta E_{\text{exch}}(t) = -h\sum_{\langle n,m\rangle}\left[\langle\hat{\mathcal{P}}_{nm}(t)\rangle - \langle\hat{\mathcal{P}}_{nm}(0)\rangle\right]. \tag{4.16}$$

At $t = 0$, only $\langle\hat{\mathcal{P}}_{23}\rangle$, $\langle\hat{\mathcal{P}}_{32}\rangle$, $\langle\hat{\mathcal{P}}_{56}\rangle$ and $\langle\hat{\mathcal{P}}_{65}\rangle$ are non-zero (since the OQN is initialized in $|\psi_1\rangle$). Their values decrease from 0.25 to ≈ 0.07 over the course of 1 ps (see Fig. B.2 in Appendix B), which makes E_{exch} increase. For the dynamics displayed in Figs. 4.1b and d, E_{exch} increases by 25.59 cm^{-1} (as calculated by Eq. 4.16). For a similar reason, E_{exch} increases for most of the parameter regimes we studied (results not shown). Considering the initial values of $\langle\hat{\mathcal{P}}_{nn}(0)\rangle$ in Eq. 4.6 and the fact that $\sum_{n=1}^{6}\langle\hat{\mathcal{P}}_{nn}(t)\rangle = 1$, the on-site energy change is (setting all BS energies to be equal, i.e., $E_{i\in\{2,3,5,6\}} = E_{BS}$)

$$\begin{aligned}\Delta E_{\text{on-site}}(t) &= \sum_{n=1}^{6} E_n\langle\hat{\mathcal{P}}_{nn}(t)\rangle - \sum_{n=1}^{6} E_n\langle\hat{\mathcal{P}}_{nn}(0)\rangle \\ &= (E_1 - E_{BS})\langle\hat{\mathcal{P}}_{11}(t)\rangle + (E_4 - E_{BS})\langle\hat{\mathcal{P}}_{44}(t)\rangle. \end{aligned}\tag{4.17}$$

From this expression, we see that the population changes of the BSs do not contribute to the on-site energy change. Since site 4 is chosen to be the exit site, E_4 is set to a lower value than E_{BS}. Thus, the higher the population of site 4, the more negative the on-site energy change will be. In fact, for the dynamics displayed in Figs. 4.1b and d, $E_{\mathrm{on-site}}$ decreases by 50.88 cm^{-1} (as calculated by Eq. 4.17), which is greater than the increase in E_{exch}. This explains the decrease in the OQN energy observed in Fig. 4.1d. In addition, Eq. 4.17 tells us that the differences $E_1 - E_{BS}$ and $E_4 - E_{BS}$ are important rather than the absolute values of E_1 and E_4. Indeed, if we shift all six site energies by the same constant, we will obtain the same population and energy change dynamics during the discharge phase (results not shown). As both $E_{\mathrm{on-site}}$ and E_{exch} rely on the quantum coordinates, when there is no change in the quantum coordinates (e.g., in the storage phase), there will be no changes in both the on-site and exchange energies.

It should be noted that, although desirable, it is not possible to separate the OQN (or system) energy into six parts corresponding to each site. Such a separation should be independent of the absolute values of the site energies. In other words, if we shift all of the site energies by a constant, the OQN energy change during the discharge phase belonging to each site should remain the same. This separation is possible for E_{exch}, e.g., one can define the exchange energy belonging to site 1 as $-\frac{h}{2}(\langle\hat{\mathcal{P}}_{12}(t)\rangle + \langle\hat{\mathcal{P}}_{21}(t)\rangle + \langle\hat{\mathcal{P}}_{16}(t)\rangle + \langle\hat{\mathcal{P}}_{61}(t)\rangle)$. However, it is not possible to divide the on-site energy in a unique way. For example, if we define the on-site energy belonging to each site to be $E_n\langle\hat{\mathcal{P}}_{nn}(t)\rangle$, then we see that the energy change $E_n(\langle\hat{\mathcal{P}}_{nn}(t)\rangle - \langle\hat{\mathcal{P}}_{nn}(0)\rangle)$ depends on the value of E_n. Therefore, we consider the OQN energy as a whole rather than attempting to decompose it into contributions from the various sites. Nonetheless, based on the expression for the OQN energy (viz., $\sum_{n=1}^{6} E_n|n\rangle\langle n| + h\sum_{\langle n,m\rangle}|n\rangle\langle m|$), it is safe to assume that the OQN energy belonging to each site will scale linearly with its population, with the slope depending on the energy gap, e.g., when $E_4 - E_{BS}$ is negative, this will result in more population on site 4 and less energy associated with site 4.

When ΔE_{exch} is comparable to $\Delta E_{\mathrm{on-site}}$, we observe a turnover in the OQN energy over the course of a trajectory [see, for example, Fig. 4.2b (900 K) and

Fig. 4.4d (100)]. This is because the exchange energy evolves at a nearly constant rate (see Fig. B in Appendix B), while the population of each site and, in turn, the on-site energy change faster in the beginning and slower at later times.

4.5.3 Effect of site energy

For the parameter set used to generate Fig. 4.1 (with $E_4 - E_{BS} = -200$ cm^{-1}), we find that the $(E_4 - E_{BS})\langle\hat{\mathcal{P}}_{44}(t)\rangle$ term in Eq. 4.17 primarily determines the on-site energy change, viz., $(E_4 - E_{BS})\langle\hat{\mathcal{P}}_{44}(t = 1 \text{ ps})\rangle = -56.37$ cm^{-1}, while $\Delta E_{on-site}(t = 1 \text{ ps}) = -50.88$ cm^{-1}. If we decrease $|E_4 - E_{BS}|$, we therefore expect the overall OQN energy loss to decrease. Indeed, this is what is observed in Fig 4.4d in going from $E_4 - E_{BS} = -200$ cm^{-1} to -100 cm^{-1}; in the latter case, the energy of the OQN only decreases by 1.12 cm^{-1} after 1 ps. It should be noted that the OQN energy change is not necessarily always negative during the discharge phase. If E_1 and E_4 are both greater than E_{BS} and the SSs become populated, then $\Delta E_{\text{on-site}}$ becomes positive. Moreover, if ΔE_{exch} also increases, the OQN will gain energy from the baths (see Fig. 4.4d).

Based on the results in Section 4.4, a few general comments are in order. Generally speaking, the higher the site energy, the lower the site population. In addition, with a higher site energy, more energy transfers from the bath to the OQN. As seen in Fig. 4.4, for the highest E_4, the (positive) OQN energy change increases and the (negative) bath energy changes decrease, while the magnitude of the SBP energy remains low and relatively constant, i.e., energy transfer from the bath to the OQN. If one changes the site energy of a particular site, then the population of that site will be mainly affected. If two sites have the same site energy, we expect them to eventually have equal populations. Finally, when all sites have the same site energy, all sites will have the same population after a sufficiently long period of time, despite starting with different initial populations (see Fig. 4.4a).

4.5.4 Effect of bath reorganization energy and temperature

As seen in Eq. 4.12, increasing the bath reorganization energy λ_b will increase the coupling strength $C_{n,j}$. For example, if we increase λ_b from 35 cm^{-1} to 70 cm^{-1}, the coupling strength for each oscillator in the bath will increase by a factor of $\sqrt{2}$. Increasing the coupling strength increases the magnitudes of the coupling terms in the equations of motion, which translates into faster energy transfer between the system and bath. As seen in Fig. 4.3b, increasing the energy transfer rate of the right bath results in more energy transfer out of the bath after 1 ps. On the other hand, increasing the energy transfer rate of the left bath does not cause any significant changes in the left bath energy and site 1 population. This may be due to the relatively low population at site 1, viz., after 1 ps, the populations at sites 1 and 4 are ≈ 0.11 and 0.28, respectively (see Fig. 4.1).

Increasing the bath temperature (or decreasing β) will increase the width of the initial Wigner distribution in Eq. 4.10, i.e., $-\sqrt{\frac{\omega_{n,j}}{2\tanh(\beta\omega_{n,j}/2)}}$. This increase is particularly significant for oscillators with low frequencies. It can be verified both analytically and numerically that the ensemble averages of the initial bath kinetic energy, $\sum_j^M P_{n,j}^2$, and bath potential energy, $\sum_j^M \omega_{n,j}^2 R_{n,j}^2$, grow linearly with increasing temperature. For example, increasing the temperature of a bath from 300 K to 600 K to 900 K will increase its kinetic energy from $\approx 1.43 \times 10^4$ eV to $\approx 2.38 \times 10^4$ eV to $\approx 3.37 \times 10^4$ eV. As seen in Fig. 4.2d, increasing the left bath or right bath temperature will lead to similar amounts of additional energy transfer out of the bath. This temperature-driven increase in energy transfer to the OQN is relatively independent of the other parameters. As seen in Fig. 4.5, for different site 4 energies, increasing the right bath temperature by a given amount leads to roughly the same increase in energy transferred from the bath to the OQN. In this way, one can decrease the OQN energy loss by increasing the temperature of any bath. Finally, varying the temperature of a given bath has a larger effect on the site connected to it. For example, if we increase the left bath temperature while keeping the right bath temperature constant, there will be a larger change in the site 1 population than the site 4 population (see Fig. 4.2). These results suggest that one could design

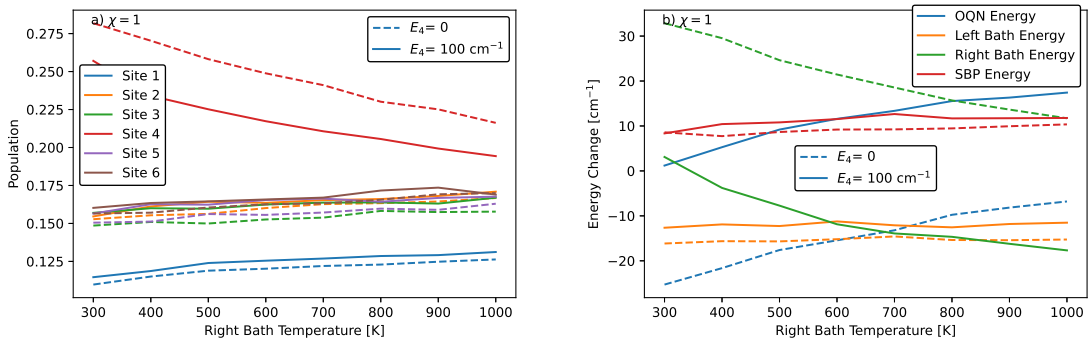

Figure 4.5: (a) Site populations and (b) energy changes after 1 ps in the discharge phase for different right bath temperatures and site 4 energies, with $E_1 = 250$ cm^{-1}, $E_{i\in\{2,3,5,6\}} = 200$ cm^{-1}, and $T_L = 300$ K.

a QB that minimizes the OQN energy loss while maintaining a relatively large site 4 population.

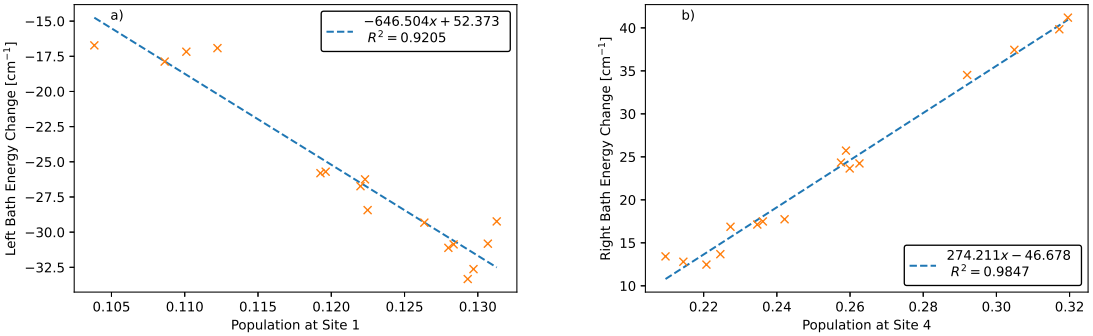

Figure 4.6: Correlation plots between bath energy changes and site populations after 1 ps for different combinations of bath temperatures and reorganization energies. (a) Left bath energy vs. site 1 population for all 16 combinations of $T_L = 300, 500, 700, 900$ K and $\lambda_{b,L} = 40, 60, 80, 100$ cm^{-1}, with $T_R = 300$ K and $\lambda_{b,R} = 35$ cm^{-1}. (b) Right bath energy vs. site 4 population for $T_R = 300, 500, 700, 900$ K and $\lambda_{b,R} = 40, 60, 80, 100$ cm^{-1}, with $T_L = 300$ K and $\lambda_{b,L} = 35$ cm^{-1}. The values of the remaining parameters are $E_1 = 250$ cm^{-1}, $E_{i\in\{2,3,5,6\}} = 200$ cm^{-1}, $E_4 = 0$ cm^{-1}, and $h = 60$ cm^{-1}. (The temperature and reorganization energy corresponding to each point are not shown.)

Finally, we noted two different linear relationships between the bath energy changes and SS populations (after 1 ps) generated from simulations performed across a wide range of bath temperatures and reorganization energies (see Fig. 4.6). The reason(s) behind these relationships is still under exploration.

Chapter 5

Conclusions and Future Work

Mixed quantum-classical dynamics is a powerful approach for simulating the dynamics of chemical and biological systems with large numbers of DOF. Among the QCLE-based methods, the DECIDE method has exhibited a highly favourable balance between computational cost and accuracy for treating model Hamiltonians expressed in complete energy bases.

In Chapter 3, we applied the DECIDE method for the first time to a simple one-dimensional, second-order Hamiltonian for a proton in a strong hydrogen bond. This required casting the DECIDE equations of motion in a finite quantum harmonic oscillator basis. We showed that for a sufficiently large basis it is possible to generate trajectories that conserve the total energy of the system. We also demonstrated the calculation of the hydrogen bond length and various energies over the course of a representative trajectory. Then, we considered a two-dimensional proton transfer model devised by Subotnik et al. [31]. This model describes the transfer of a proton between a donor and an acceptor group, mediated by a solvent coordinate. We first found a suitable parameter set to yield adiabatic potential energy surfaces with a conical intersection between the ground and first-excited state surfaces. Then, we cast the DECIDE equations of motion for this model in a quantum harmonic oscillator basis and simulated its dynamics. Although the resulting trajectories appeared to be qualitatively reasonable, the total energy was not conserved beyond very short times. A detailed analysis revealed that the breakdown in energy conservation was due to the

incompleteness of the basis set, which is inherent to the position representation, and the higher order (i.e., cubic, quartic) terms in the Hamiltonian. This indicated that a finite position basis is not suitable for representing the DECIDE equations of motion for Hamiltonians with cubic or higher order terms, and therefore an alternative approach is needed.

In Chapter 4, we explored the population and energy dynamics of a quantum battery model, originally proposed in Ref. [30], over a wide parameter regime. In the battery's storage phase, we demonstrated that, in addition to no population leakage, there is no energy leakage from the battery into the connected baths. During the discharge phase, the changes in the battery energy are determined by the energy gap between BSs and SSs rather than the absolute value of each site energy. When the energy of the exit site is lower than those of the BSs, the battery energy decreases in most of the parameter regimes we studied. Lowering a given site energy causes the corresponding site population to increase. When the site energies are equal, the site populations reach roughly equal values after 1 ps, despite the different initial populations.

With regards to the effect of the bath parameters, increasing the bath temperature increases the width of the initial Wigner distribution, while increasing the bath reorganization energy only changes the coupling strengths. Varying the parameters of a given bath has a larger effect on the site the bath is directly connected to. We also observed a linear relationship between the bath energy changes and the site populations, which depend on the site energy gaps.

The choice of parameters for the quantum battery model can be made depending on the desired purpose for the battery. For example, for an energy battery, one may like the battery to gain energy from its environment during the discharge phase. In such a case, if one could make the energies of the SSs greater than those of the BSs, this would ensure that the battery gains energy and the SS populations continue to increase. On the other hand, for an excitonic battery, one may like to maximize the population of the exit site, regardless of the change in battery energy. In such a case, one could lower the exit site energy, or lower the temperature of the right bath while maintaining the original temperature of the left bath. If one requires a

quantum battery with little loss in battery energy and a higher exit site population, one could either increase the exit site energy or increase the temperature of the left bath. This would lead to more energy transfer out of the left bath to mitigate the loss in battery energy.

In this work, we have demonstrated the ability of our quantum battery model to serve as an energy/exciton storage device. However, ways to harness the stored energy/exciton have yet to be explored. In principle, this could be done by attaching the battery to a sink to extract the energy/exciton during the discharge phase. By giving an explicit form to the sink, one may begin to study QB-powered processes. In addition, in this work, we used a uniform nearest-neighbor electronic coupling strength between each site. However, it is possible to use non-uniform coupling strengths while preserving the symmetry and dissipationless dynamics of the system during the storage phase. Thus, future work will investigate the dynamics resulting from the use of non-uniform and time-dependent coupling strengths.

Bibliography

[1] John C Tully. Mixed quantum–classical dynamics. *Faraday Discussions*, 110:407–419, 1998.

[2] Raymond Kapral and Giovanni Ciccotti. Mixed quantum-classical dynamics. *The Journal of chemical physics*, 110(18):8919–8929, 1999.

[3] Raymond Kapral. Progress in the theory of mixed quantum-classical dynamics. *Annual Review of Physical Chemistry*, 57:129–157, 2006.

[4] Gabriel Hanna and Raymond Kapral. Quantum-classical liouville dynamics of nonadiabatic proton transfer. *The Journal of chemical physics*, 122(24):244505, 2005.

[5] Sharon Hammes-Schiffer and John C Tully. Proton transfer in solution: Molecular dynamics with quantum transitions. *The Journal of chemical physics*, 101(6):4657–4667, 1994.

[6] Najeh Rekik, Chang-Yu Hsieh, Holly Freedman, and Gabriel Hanna. A mixed quantum-classical liouville study of the population dynamics in a model photo-induced condensed phase electron transfer reaction. *The Journal of chemical physics*, 138(14):144106, 2013.

[7] Farnaz A Shakib and Gabriel Hanna. New insights into the nonadiabatic state population dynamics of model proton-coupled electron transfer reactions from the mixed quantum-classical liouville approach. *The Journal of chemical physics*, 144(2):024110, 2016.

[8] Jian-Yun Fang and Sharon Hammes-Schiffer. Proton-coupled electron transfer reactions in solution: molecular dynamics with quantum transitions for model systems. *The Journal of chemical physics*, 106(20):8442–8454, 1997.

[9] Jian-Yun Fang and Sharon Hammes-Schiffer. Excited state dynamics with nonadiabatic transitions for model photoinduced proton-coupled electron transfer reactions. *The Journal of chemical physics*, 107(15):5727–5739, 1997.

[10] Jian-Yun Fang and Sharon Hammes-Schiffer. Nonadiabatic dynamics for processes involving multiple avoided curve crossings: Double proton transfer and proton-coupled electron transfer reactions. *The Journal of chemical physics*, 107(21):8933–8939, 1997.

[11] Alexander V Soudackov and Sharon Hammes-Schiffer. Removal of the double adiabatic approximation for proton-coupled electron transfer reactions in solution. *Chemical physics letters*, 299(5):503–510, 1999.

[12] Farnaz A Shakib and Gabriel Hanna. An analysis of model proton-coupled electron transfer reactions via the mixed quantum-classical liouville approach. *The Journal of chemical physics*, 141(4):044122, 2014.

[13] Farnaz Shakib and Gabriel Hanna. Mixed quantum-classical liouville approach for calculating proton-coupled electron-transfer rate constants. *Journal of chemical theory and computation*, 12(7):3020–3029, 2016.

[14] Elvira R Sayfutyarova, Joshua J Goings, and Sharon Hammes-Schiffer. Electron-coupled double proton transfer in the slr1694 bluf photoreceptor: A multireference electronic structure study. *The Journal of Physical Chemistry B*, 123(2):439–447, 2018.

[15] Gitt Panitchayangkoon, Dmitri V Voronine, Darius Abramavicius, Justin R Caram, Nicholas HC Lewis, Shaul Mukamel, and Gregory S Engel. Direct evidence of quantum transport in photosynthetic light-harvesting complexes. *Proceedings of the National Academy of Sciences*, 108(52):20908–20912, 2011.

[16] Aaron Kelly and Young Min Rhee. Mixed quantum-classical description of excitation energy transfer in a model fenna- matthews- olsen complex. *The Journal of Physical Chemistry Letters*, 2(7):808–812, 2011.

[17] Elinor Zerah Harush and Yonatan Dubi. Do photosynthetic complexes use quantum coherence to increase their efficiency? probably not. *Science Advances*, 7(8):eabc4631, 2021.

[18] Dvira Segal and Bijay Kumar Agarwalla. Vibrational heat transport in molecular junctions. *Annual review of physical chemistry*, 67:185–209, 2016.

[19] Junjie Liu, Chang-Yu Hsieh, Dvira Segal, and Gabriel Hanna. Heat transfer statistics in mixed quantum-classical systems. *The Journal of chemical physics*, 149(22):224104, 2018.

[20] Pablo Carpio-Martínez and Gabriel Hanna. Nonequilibrium heat transport in a molecular junction: A mixed quantum-classical approach. *The Journal of chemical physics*, 151(7):074112, 2019.

[21] Aaron Kelly. Mean field theory of thermal energy transport in molecular junctions. *The Journal of chemical physics*, 150(20):204107, 2019.

[22] Raymond Kapral. Quantum dynamics in open quantum-classical systems. *Journal of Physics: Condensed Matter*, 27(7):073201, 2015.

[23] Donal Mac Kernan, Giovanni Ciccotti, and Raymond Kapral. Trotter-based simulation of quantum-classical dynamics. *The Journal of Physical Chemistry B*, 112(2):424–432, 2008.

[24] Junjie Liu and Gabriel Hanna. Efficient and deterministic propagation of mixed quantum-classical liouville dynamics. *The journal of physical chemistry letters*, 9(14):3928–3933, 2018.

[25] Ali Nassimi, Sara Bonella, and Raymond Kapral. Analysis of the quantum-classical liouville equation in the mapping basis. *The Journal of chemical physics*, 133(13):134115, 2010.

[26] Aaron Kelly, Ramses van Zon, Jeremy Schofield, and Raymond Kapral. Mapping quantum-classical liouville equation: Projectors and trajectories. *The Journal of chemical physics*, 136(8):084101, 2012.

[27] Hyun Woo Kim and Young Min Rhee. Improving long time behavior of poisson bracket mapping equation: A non-hamiltonian approach. *The Journal of chemical physics*, 140(18):184106, 2014.

[28] Junjie Liu, Dvira Segal, and Gabriel Hanna. Hybrid quantum-classical simulation of quantum speed limits in open quantum systems. *Journal of Physics A: Mathematical and Theoretical*, 52(21):215301, 2019.

[29] Pablo Carpio-Martínez and Gabriel Hanna. Quantum bath effects on nonequilibrium heat transport in model molecular junctions. *The Journal of Chemical Physics*, 154(9):094108, 2021.

[30] Junjie Liu, Dvira Segal, and Gabriel Hanna. Loss-free excitonic quantum battery. *The Journal of Physical Chemistry C*, 123(30):18303–18314, 2019.

[31] Amber Jain, Ethan Alguire, and Joseph E. Subotnik. An efficient, augmented surface hopping algorithm that includes decoherence for use in large-scale simulations. *Journal of Chemical Theory and Computation*, 12(11):5256–5268, 2016. PMID: 27715036.

[32] Eugene P Wigner. On the quantum correction for thermodynamic equilibrium. In *Part I: Physical Chemistry. Part II: Solid State Physics*, pages 110–120. Springer, 1997.

[33] William B Case. Wigner functions and weyl transforms for pedestrians. *American Journal of Physics*, 76(10):937–946, 2008.

[34] Kaya Imre, Ercüment Özizmir, Marcos Rosenbaum, and PF Zweifel. Wigner method in quantum statistical mechanics. *Journal of Mathematical Physics*, 8(5):1097–1108, 1967.

[35] Thomas L Curtright, David B Fairlie, and Cosmas K Zachos. *A concise treatise on quantum mechanics in phase space*. World Scientific Publishing Company, 2013.

[36] José E Moyal. Quantum mechanics as a statistical theory. In *Mathematical Proceedings of the Cambridge Philosophical Society*, volume 45, pages 99–124. Cambridge University Press, 1949.

[37] Ali M Nassimi. *A study of quantum-classical dynamics in the mapping basis*. PhD thesis, University of Toronto, 2011.

[38] Endre Süli and David F Mayers. *An introduction to numerical analysis*. Cambridge university press, 2003.

[39] H Azzouz and D Borgis. A quantum molecular-dynamics study of proton-transfer reactions along asymmetrical h bonds in solution. *The Journal of chemical physics*, 98(9):7361–7374, 1993.

[40] Heinz-Peter Breuer, Francesco Petruccione, et al. *The theory of open quantum systems*. Oxford University Press on Demand, 2002.

[41] Ulrich Weiss. *Quantum dissipative systems*, volume 13. World scientific, 2012.

[42] Inés De Vega and Daniel Alonso. Dynamics of non-markovian open quantum systems. *Reviews of Modern Physics*, 89(1):015001, 2017.

[43] Daniel A Lidar. Review of decoherence-free subspaces, noiseless subsystems, and dynamical decoupling. *Quantum Information and Computation for Chemistry*, pages 295–354, 2014.

[44] Andrzej Jamiołkowski, Takeo Kamizawa, and Grzegorz Pastuszak. On invariant subspace in quantum control systems and some concepts of integrable quantum systems. *International Journal of Theoretical Physics*, 54(8):2662–2674, 2015.

[45] Berislav Buča and Tomaž Prosen. A note on symmetry reductions of the lindblad equation: transport in constrained open spin chains. *New Journal of Physics*, 14(7):073007, 2012.

[46] Juzar Thingna, Daniel Manzano, and Jianshu Cao. Dynamical signatures of molecular symmetries in nonequilibrium quantum transport. *Scientific reports*, 6(1):1–11, 2016.

[47] Victor V Albert and Liang Jiang. Symmetries and conserved quantities in lindblad master equations. *Physical Review A*, 89(2):022118, 2014.

[48] Dieter Suter and Gonzalo A Álvarez. Colloquium: Protecting quantum information against environmental noise. *Reviews of Modern Physics*, 88(4):041001, 2016.

[49] Paolo Zanardi and Mario Rasetti. Noiseless quantum codes. *Physical Review Letters*, 79(17):3306, 1997.

[50] Daniel A Lidar, Isaac L Chuang, and K Birgitta Whaley. Decoherence-free subspaces for quantum computation. *Physical Review Letters*, 81(12):2594, 1998.

[51] Daniel A Lidar and K Birgitta Whaley. Decoherence-free subspaces and subsystems. In *Irreversible quantum dynamics*, pages 83–120. Springer, 2003.

[52] Almut Beige, Daniel Braun, Ben Tregenna, and Peter L Knight. Quantum computing using dissipation to remain in a decoherence-free subspace. *Physical review letters*, 85(8):1762, 2000.

[53] Peng Xue and Yun-Feng Xiao. Universal quantum computation in decoherence-free subspace with neutral atoms. *Physical review letters*, 97(14):140501, 2006.

[54] Stefano Gherardini, Francesco Campaioli, Filippo Caruso, and Felix C Binder. Stabilizing open quantum batteries by sequential measurements. *Physical Review Research*, 2(1):013095, 2020.

[55] Gonzalo Manzano, Gian-Luca Giorgi, Rosario Fazio, and Roberta Zambrini. Boosting the performance of small autonomous refrigerators via common environmental effects. *New Journal of Physics*, 21(12):123026, 2019.

[56] Daniel Manzano and Pablo I Hurtado. Symmetry and the thermodynamics of currents in open quantum systems. *Physical Review B*, 90(12):125138, 2014.

[57] Dvira Segal and Abraham Nitzan. Spin-boson thermal rectifier. *Physical review letters*, 94(3):034301, 2005.

[58] Dvira Segal and Abraham Nitzan. Heat rectification in molecular junctions. *The Journal of chemical physics*, 122(19):194704, 2005.

[59] Zhaohui Wang, Jeffrey A Carter, Alexei Lagutchev, Yee Kan Koh, Nak-Hyun Seong, David G Cahill, and Dana D Dlott. Ultrafast flash thermal conductance of molecular chains. *science*, 317(5839):787–790, 2007.

[60] Nehad Ali Shah, IL Animasaun, Jae Dong Chung, Abderrahim Wakif, FI Alao, and CSK Raju. Significance of nanoparticle's radius, heat flux due to concentration gradient, and mass flux due to temperature gradient: the case of water conveying copper nanoparticles. *Scientific Reports*, 11(1):1–11, 2021.

[61] Abdelkrim Trabelsi, Rafik Belarbi, Kamilia Abahri, and Menghao Qin. Assessment of temperature gradient effects on moisture transfer through thermogradient coefficient. In *Building Simulation*, volume 5, pages 107–115. Springer, 2012.

[62] J. Frenkel. On the transformation of light into heat in solids. i. *Phys. Rev.*, 37:17–44, Jan 1931.

[63] Volkhard May and Oliver Kühn. *Charge and energy transfer dynamics in molecular systems*. John Wiley & Sons, 2008.

[64] Álvaro Tejero, Juzar Thingna, and Daniel Manzano. Comment on "loss-free excitonic quantum battery". *The Journal of Physical Chemistry C*, 125(13):7518–7520, 2021.

[65] D Manzano and PI Hurtado. Harnessing symmetry to control quantum transport. *Advances in Physics*, 67(1):1–67, 2018.

[66] Haobin Wang, Michael Thoss, and William H Miller. Systematic convergence in the dynamical hybrid approach for complex systems: A numerically exact methodology. *The Journal of Chemical Physics*, 115(7):2979–2990, 2001.

[67] Pengfei Huo and David F Coker. Semi-classical path integral non-adiabatic dynamics: a partial linearized classical mapping hamiltonian approach. *Molecular Physics*, 110(9-10):1035–1052, 2012.

[68] Akihito Ishizaki and Graham R Fleming. Theoretical examination of quantum coherence in a photosynthetic system at physiological temperature. *Proceedings of the National Academy of Sciences*, 106(41):17255–17260, 2009.

[69] E Baylis Shanks. Higher order approximations of runge-kutta type. 1965.

[70] Harald JW Müller-Kirsten. *Introduction to Quantum Mechanics: Schrödinger Equation and Path Integral*. World Scientific Publishing Company, 2006.

Appendices

A Parameter determination for 2D proton transfer model

The goal was to obtain similar potential energy surface slices to those in Fig. 7d in Ref. [31]. This was accomplished using the same values of A^0 (-3367.6 cm^{-1} Å^{-2}) and B^0 (133501.2 cm^{-4} Å^{-2}) as in Ref. [31]. For the masses, we used $m = 1$ amu and $M = 200$ amu. To set the remainder of the parameter values, we took the following steps. First, we chose $X_2 = 0.18$ and only considered V_0 and V_c. For $X_1 = 0$, the potential energy surface has a symmetric double-well profile. The depth (i.e., difference between the energy at $x = 0$ and x_{min}) of the potential is $\frac{A^0+k_2X_2^2}{4B^0}$, where $A^0 + k_2X_2$ is a negative value ensuring the existence of minima. We set k_2 to be a negative number and, as the value of k_2 is decreased, the wells become deeper. When the wells become deeper, the energy difference between the ground and first-excited states become closer. Figure A.1a shows the variational energy of the first five states as a function of k_2, while Fig. A.1b shows the energy difference between the ground and first-excited states as a function of k_2. The analytical energy difference for the double-well potential $V(x) = -\frac{1}{4}h^4x^2 + \frac{1}{2}c^2x^4$ is [70]

$$\Delta E = 2^{9/4}\frac{h^5}{\sqrt{\pi}c}e^{-\frac{h^6}{6\sqrt{2}c^2}}, \tag{A.1}$$

A schematic plot of this difference as a function of h^4 is shown in Fig. A.1c. As can be seen, when h^4 is large enough, the energy gap between the first two states decreases with increasing h^4, which is in agreement with the result in Fig. A.1b. Based on our calculations, to obtain nearly degenerate ground state energies, the value of k_2 should be around -2×10^5 cm^{-1} Å^{-3}. Thus, we chose $k_2 = -2 \times 10^5$ cm^{-1} Å^{-3}.

The next step was to determine the value of k_1. The coefficient of the first order term in x is k_1X_1. The effect of this term is to make the double-well potential asymmetric and, for some values, one of the two minima of the potential disappears. Since the coefficient of x is k_1X_1, simply varying k_1 will not affect the shape of the potential, but just stretches it over the range of X_1. Figure A.1d shows the potential

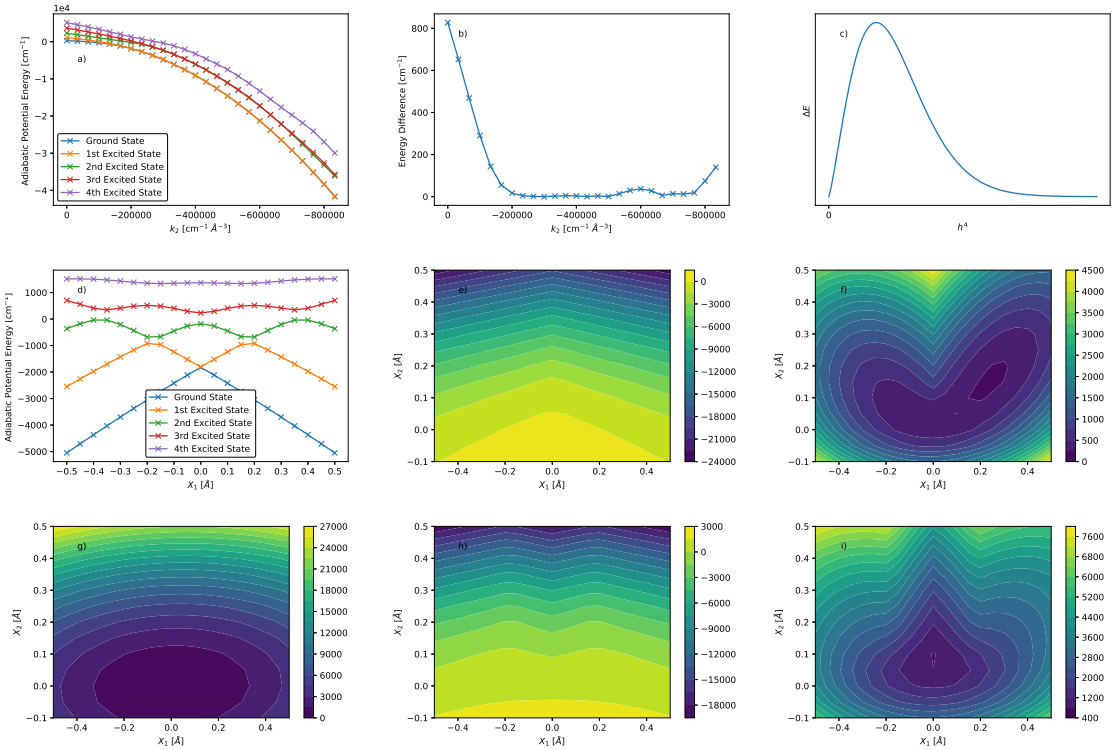

Figure A.1: Steps for determining the parameter values in the 2D proton transfer model: (1) Vary k_2 (a-c), (2) Fix $k_2 = -2 \times 10^5$ cm^{-1} Å^{-3} to determine k_1 (d), and (3) Determine k_3, ω_1, and ω_2 (e-i). (a) Variational energy, $\left\langle \Psi_n | \frac{\hat{p}^2}{2m} + V_0 + V_c | \Psi_n \right\rangle$, of the first five energy levels as a function of k_2, with $X_1 = 0$ and $X_2 = 0.18$ Å. Note the y-axis ranges from -4×10^4 to 0. (b) Difference between the ground and first-excited state energies in (a). (c) Difference between the ground and first-excited state energy as a function of the coefficient of the second-order term in Eq. 5.1. (d) 1D slices along X_2 =0.18 Å of the first five adiabatic potential energy surfaces, $\langle \Psi_n | \frac{\hat{p}^2}{2m} + V_0 + V_c | \Psi_n \rangle$, as a function of X_1. (e) Ground-state adiabatic potential energy surface, $\langle \Psi_0 | \frac{\hat{p}^2}{2m} + V_0 + V_c | \Psi_0 \rangle$, as a function of X_1 and X_2. (f) Ground-state adiabatic potential energy surface including V_1, $\langle \Psi_0 | \frac{\hat{p}^2}{2m} + V_0 + V_c | \Psi_0 \rangle + V_1$, as a function of X_1 and X_2. (g) Contour plot of V_1, as a function of X_1 and X_2. (h) First-excited state adiabatic potential energy surface, $\langle \Psi_1 | \frac{\hat{p}^2}{2m} + V_0 + V_c | \Psi_1 \rangle$, as a function of X_1 and X_2. (i) First-excited adiabatic potential energy surface including V_1, $\langle \Psi_1 | \frac{\hat{p}^2}{2m} + V_0 + V_c | \Psi_1 \rangle + V_1$, as a function of X_1 and X_2. All surfaces were generated with 16 harmonic oscillator basis functions, $k_1 = 1.7 \times 10^4$ cm^{-1} Å^{-2}, and $k_2 = -2 \times 10^5$ cm^{-1} Å^{-3}. Units of energy are cm^{-1}.

surface with respect to X_1. We chose $k_1 = 1.7 \times 10^4$ cm^{-1} Å^{-2}, as this value ensures that the desired three local minima (as seen in Fig. 3.5) exist in the third excited state potential when $-0.5 < X_1 < 0.5$. If k_1 is too large or too small, the number of minima will be different.

Now we can add V_1 into our consideration to find appropriate values for k_3, ω_1, and ω_2. As there are no quantum variables in V_1, we can calculate its value directly. V_1 alters the shape of the potential surface. For example, without V_1, the ground state energy always decreases when X_1 is away from the center. By introducing V_1, there are now two minima in the ground state. The value of ω_1 determines the positions of the two minima. We chose $\omega_1 = 13560.98$ cm^{-1}. Similarly, we chose the value of ω_2 to be 90312.43 cm^{-1}. The addition of k_3X makes the potential energy surface no longer symmetric about the y-axis. By adjusting the positions of the two minima in Fig. A.1f, we found $k_3 = -4 \times 10^3$ cm^{-1} Å^{-2}.

B Appendix to Chapter 4

Total Energy Drift

Here we show the total energy as a function of time for the QB model. As can be seen in the figure, the total energy drift is less than 1×10^{-2} cm^{-1}.

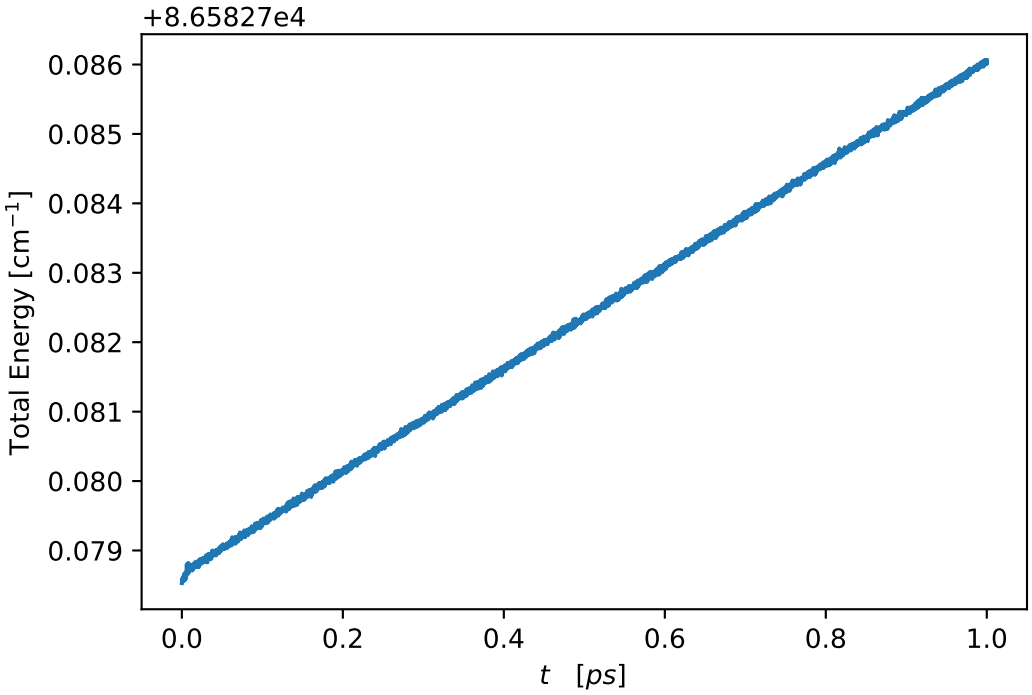

Figure B.1: Average total energy as a function of time during the discharge phase. The average was calculated using an ensemble of 10,000 trajectories. All parameter values are the same as in the caption of Fig. 4.1.

Effect of Varying SS Energies

Table B.1: Site populations and energy changes during the discharge phase after 1 ps for different values of E_1 and E_4 with $E_{i\in\{2,3,5,6\}} = 200$ cm^{-1}.

E_n of SSs		Site Populations						Energy Changes [cm^{-1}]			
E_1	E_4	Site 1	Site 2	Site 3	Site 4	Site 5	Site 6	System	Left Bath	Right Bath	Probe
250	0	0.1098	0.1528	0.1486	0.2818	0.1505	0.1565	-25.2871	-16.1494	32.8629	8.5810
400	250	0.0549	0.1967	0.2050	0.1453	0.2033	0.1949	30.5251	-10.3941	-26.5583	6.4347
100	100	0.2166	0.1441	0.1411	0.2139	0.1423	0.1419	-22.1795	7.5300	6.3110	8.3458
200	200	0.1617	0.1698	0.1720	0.1584	0.1711	0.1670	16.9965	-13.7518	-12.1952	8.9579
250	250	0.1312	0.1859	0.1848	0.1296	0.1857	0.1827	28.0908	-18.6962	-17.5048	8.1177
200	50	0.1393	0.1472	0.1445	0.2703	0.1491	0.1496	-17.1695	-9.5391	18.8073	7.9086
250	100	0.1146	0.1546	0.1570	0.2570	0.1565	0.1603	1.1991	-12.6415	3.1000	8.3498
150	0	0.1725	0.1419	0.1381	0.2619	0.1410	0.1447	-34.9490	-4.2506	30.8475	8.3595

Derivation of Eq. 4.15

Here we show the steps for deriving the expression for the time derivative of the bath energy matrix elements given in Eq. 4.15 of the main text.

$$
\begin{aligned}
\frac{d}{dt}[H_B + \hat{H}_{NB}]^{\beta\beta'} &= \frac{1}{2}\sum_j^M \frac{d}{dt}\left[P_{n,j}^2 + \omega_{n,j}^2 R_{n,j}^2 + \frac{C_{n,j}^2}{\omega_{n,j}^2}\hat{\mathcal{P}}_{nn} - C_{n,j}R_{n,j}\hat{\mathcal{P}}_{nn} - C_{n,j}\hat{\mathcal{P}}_{nn}R_{n,j}\right]^{\beta\beta'} \\
&= \frac{1}{2}\sum_j^M \left[P_{n,j}\frac{d}{dt}P_{n,j} + \left(\frac{d}{dt}P_{n,j}\right)P_{n,j} + \omega_{n,j}^2 R_{n,j}\frac{d}{dt}R_{n,j} + \omega_{n,j}^2\left(\frac{d}{dt}R_{n,j}\right)R_{n,j}\right. \\
&\quad + \frac{C_{n,j}^2}{\omega_{n,j}^2}\frac{d}{dt}\hat{\mathcal{P}}_{nn} - C_{n,j}\left(\frac{d}{dt}R_{n,j}\right)\hat{\mathcal{P}}_{nn} - C_{n,j}\hat{\mathcal{P}}_{nn}\frac{d}{dt}R_{n,j} \\
&\quad \left. - C_{n,j}R_{n,j}\frac{d}{dt}\hat{\mathcal{P}}_{nn} - C_{n,j}\left(\frac{d}{dt}\hat{\mathcal{P}}_{nn}\right)R_{n,j}\right]^{\beta\beta'} \\
&= \frac{1}{2}\sum_j^M \left[P_{n,j}\left(-\omega_{n,j}^2 R_{n,j} + C_{n,j}\hat{\mathcal{P}}_{nn}\right) + \left(-\omega_{n,j}^2 R_{n,j} + C_{n,j}\hat{\mathcal{P}}_{nn}\right)P_{n,j}\right. \\
&\quad + \omega_{n,j}^2 R_{n,j}P_{n,j} + \omega_{n,j}^2 P_{n,j}R_{n,j} + \frac{C_{n,j}^2}{\omega_{n,j}^2}\frac{d}{dt}\hat{\mathcal{P}}_{nn} \\
&\quad \left. - C_{n,j}P_{n,j}\hat{\mathcal{P}}_{nn} - C_{n,j}\hat{\mathcal{P}}_{nn}P_{n,j} - C_{n,j}R_{n,j}\frac{d}{dt}\hat{\mathcal{P}}_{nn} - C_{n,j}\left(\frac{d}{dt}\hat{\mathcal{P}}_{nn}\right)R_{n,j}\right]^{\beta\beta'} \\
&= \frac{1}{2}\sum_j \left[\frac{C_{n,j}^2}{\omega_{n,j}^2}\frac{d}{dt}\hat{\mathcal{P}}_{nn} - C_{n,j}R_{n,j}\frac{d}{dt}\hat{\mathcal{P}}_{nn} - C_{n,j}\left(\frac{d}{dt}\hat{\mathcal{P}}_{nn}\right)R_{n,j}\right]^{\beta\beta'},
\end{aligned}
$$

which yields Eq. 4.15. To arrive at the third equality, we substituted the equations of motion in Eq. 4.9. Substituting the expressions for $C_{n,j}$ and $\omega_{n,j}$ from Eqs. 4.11 and 4.12 yields the bath-specific form of the time derivative of the expectation value of the bath energy,

$$\begin{aligned}\frac{d}{dt}\langle H_B + \hat{H}_{NB}\rangle &= \frac{2}{\pi}\lambda_b \arctan(\omega_{max}/\omega_c)\frac{d}{dt}\langle\hat{\mathcal{P}}_{nn}(t)\rangle \\ &\quad -\frac{1}{2}\sum_j C_{n,j}\left[R_{n,j}\frac{d}{dt}\langle\hat{\mathcal{P}}_{nn}(t)\rangle + \left(\frac{d}{dt}\langle\hat{\mathcal{P}}_{nn}(t)\rangle\right)R_{n,j}\right].\end{aligned}$$

Time-dependent Quantum Coordinates

Here we provide a figure showing the values of the time-dependent quantum coordinates during the discharge phase. It should be noted that by using these values and Eq. 4.16, one can calculate $\Delta E_{\text{exch}}(t)$.

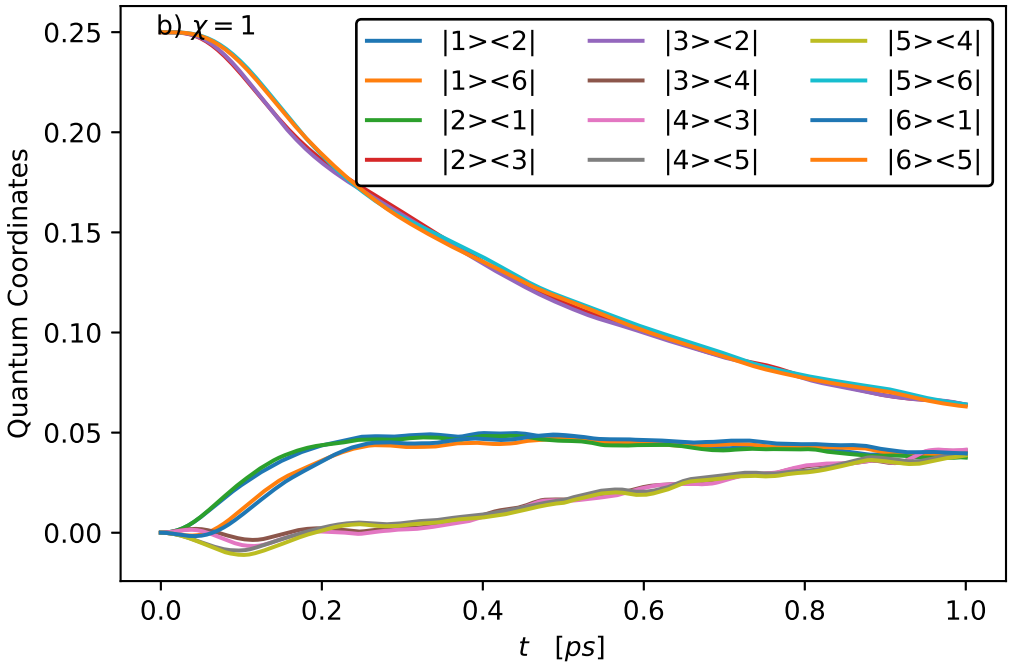

Figure B.2: Time-dependence of expectation values of off-diagonal quantum coordinates during the discharge phase. Ensemble averages were taken over 10,000 trajectories. All parameter values are the same as in the caption of Fig. 4.1.